

UNCLASSIFIED

SECURITY CLASSIFICATION OF THIS PAGE (When Data Entered)

REPORT DOCUMENTATION PAGE		READ INSTRUCTIONS BEFORE COMPLETING FORM
1. REPORT NUMBER NORDA Report 60	2. GOVT ACCESSION NO.	3. RECIPIENT'S CATALOG NUMBER
4. TITLE (and Subtitle) The Use of Principal Components Analysis Techniques on Nimbus-7 Coastal Zone Color Scanner Data to Define Mesoscale Ocean Features through a Warm, Humid Atmosphere		5. TYPE OF REPORT & PERIOD COVERED Final
7. AUTHOR(s) Ronald J. Holyer Paul E. La Violette		6. PERFORMING ORG. REPORT NUMBER
9. PERFORMING ORGANIZATION NAME AND ADDRESS Naval Ocean Research and Development Activity Ocean Science Directorate NSTL, Mississippi 39529		8. CONTRACT OR GRANT NUMBER(s)
11. CONTROLLING OFFICE NAME AND ADDRESS Same		10. PROGRAM ELEMENT, PROJECT, TASK AREA & WORK UNIT NUMBERS P.E. 62759N
12. REPORT DATE April 1984		13. NUMBER OF PAGES 64
14. MONITORING AGENCY NAME & ADDRESS (if different from Controlling Office)		15. SECURITY CLASS. (of this report) UNCLASSIFIED
		15a. DECLASSIFICATION/DOWNGRADING SCHEDULE
16. DISTRIBUTION STATEMENT (of this Report) Approved for Public Release. Distribution Unlimited.		
17. DISTRIBUTION STATEMENT (of the abstract entered in Block 20, if different from Report)		
18. SUPPLEMENTARY NOTES		
19. KEY WORDS (Continue on reverse side if necessary and identify by block number) Coastal Zone Color Scanner (CZCS) satellite Principal Components Analysis Nimbus-7 ocean features		
20. ABSTRACT (Continue on reverse side if necessary and identify by block number) The Nimbus-7 Coastal Zone Color Scanner (CZCS) has the unique potential to remotely sense mesoscale ocean features through warm, humid atmospheres that are opaque to thermal infrared sensors. The major obstacle to the use of these data is the masking effect of sunlight backscattered by the atmosphere. This study details a new atmospheric correction method, employing principal component analysis techniques, that effectively removes the atmospheric radiance from CZCS images of the ocean. The method has the advantage of ease of use and,		

UNCLASSIFIED

SECURITY CLASSIFICATION OF THIS PAGE (When Data Entered)

hence, allows the CZCS data to be incorporated into routine naval environmentally oriented operations. The study shows the method to be especially effective in the descriptive analyses of mesoscale oceanic phenomena. Four examples of the use of the technique are presented for three different ocean areas.

UNCLASSIFIED

SECURITY CLASSIFICATION OF THIS PAGE(When Data Entered)

The Use of Principal Components Analysis Techniques on Nimbus-7 Coastal Zone Color Scanner Data to Define Mesoscale Ocean Features through a Warm, Humid Atmosphere

Ronald J. Holyer
Paul E. La Violette

Ocean Science Directorate
Ocean Sensing and Prediction Division

April 1984



Approved for Public Release
Distribution Unlimited

Naval Ocean Research and Development Activity
NSTL, Mississippi 39529

Foreword

One of the Major problems in using satellite data to study mesoscale ocean features is that of atmospheric backscattering of sunlight, which has a masking effect on the data.

This report deals with a new atmospheric correction method, used with the Nimbus-7 Coastal Zone Color Scanner (CZCS), that effectively removes atmospheric radiance from the satellite images. The method employed is Principal Components Analysis, a statistical tool used in the field of pattern recognition.

This method is easy to use and allows CZCS data to be incorporated into routine naval environment-oriented operations. This report presents four examples for three ocean areas.

G. T. Phelps

G. T. Phelps, Captain, USN
Commanding Officer, NORDA

Executive Summary

The Nimbus-7 Coastal Zone Color Scanner (CZCS) has the unique potential to remotely sense mesoscale ocean features through warm, humid atmospheres that are opaque to thermal infrared sensors. The major obstacle to the use of these data is the masking effect of sunlight backscattered by the atmosphere. This study details a new atmospheric correction method, employing principal component analysis techniques, that effectively removes the atmospheric radiance from CZCS images of the ocean. The method has the advantage of ease of use and, hence, allows the CZCS data to be incorporated into routine naval environmentally-oriented operations. The study shows the method to be especially effective in the descriptive analyses of mesoscale oceanic phenomena. Four examples of the use of the technique are presented for three different ocean areas.

Acknowledgments

This work was funded by ONR program element 61153N, "Satellite Measurements of Ocean Optical Properties," and by NAVAIR program element 62759N, "Ocean Optical Techniques."

The authors wish to acknowledge the conscientious efforts of Sarah Peckinpaugh, Sam Oriel, and Nita Chase of Computer Sciences Corporation who performed the processing of satellite data for this report.

The NORDA Code 321 Interactive Digital Satellite Image Processing System (IDSIPS) was used for all image processing.

Contents

ILLUSTRATIONS	v
1. INTRODUCTION	1
2. ATMOSPHERIC CORRECTION TECHNIQUES: THE SINGLE-SCATTERING METHOD	7
2.1 THE SINGLE-SCATTERING APPROXIMATION	7
2.2 ASSUMPTIONS ABOUT OCEANIC SPECTRAL RADIANCE	7
2.3 ASSUMPTIONS ABOUT THE UNCERTAINTY IN SPECTRAL DISTRIBUTION OF AEROSOL BACKSCATTER	8
2.4 THE SINGLE-SCATTERING MODEL APPLIED TO A TEST CASE	9
3. ATMOSPHERIC CORRECTION TECHNIQUES: PRINCIPAL COMPONENTS ANALYSIS METHOD	13
3.1 PRINCIPAL COMPONENTS ANALYSIS	13
3.2 STATISTICS OF THE TEST CASE DATA	14
3.3 CORRECTED IMAGERY	16
3.4 ATMOSPHERIC CORRECTION SUMMARY	16
4. CZCS CASE STUDIES	17
4.1 CASE I--GRAND BANKS	19
4.1.1 The Surface Data	19
4.1.2 The CZCS Data	19
4.1.3 Discussion of Case I	20
4.2 CASE II--GULF OF MEXICO (SUMMER)	22
4.2.1 The Surface Data	25
4.2.2 The CZCS Data	26
4.2.3 Discussion of Case II	29
4.3 CASE III--GULF OF MEXICO (WINTER)	30
4.3.1 The Surface Data	30
4.3.2 The CZCS Data	41
4.3.3 Discussion of Case III	41

4.4 CASE IV--MEDITERRANEAN	41
4.4.1 The Surface Data	41
4.4.2 The CZCS Data	47
4.4.3 Discussion of Case IV	52
5. UNIVERSAL QUICK-LOOK CZCS ATMOSPHERIC CORRECTION ALGORITHMS	52
6. SUMMARY AND CONCLUSIONS	58
7. REFERENCES	62

Illustrations

Figure 1.	NOAA-7 thermal-IR ($11.0\ \mu$) image of the Gulf of Mexico for 10 December 1981.	2
Figure 2.	TIROS-N thermal-IR ($11.0\ \mu$) image of the Gulf of Mexico for 24 June 1979.	3
Figure 3.	TIROS-N thermal-IR ($11.0\ \mu$) image of the Gulf of Mexico for 19 June 1979.	4
Figure 4.	Color image formed from CZCS channels 1, 2, and 3.	5
Figure 5.	Spectral radiance of the ocean measured just above sea surface.	8
Figure 6.	Aerosol optical depth of a vertical atmospheric path in the Gulf of Mexico.	9
Figure 7.	Image of CZCS channel 6 (infrared data) coincident with Figure 4.	10
Figure 8.	Color image formed by atmospherically corrected CZCS channels 1, 2, and 3.	12
Figure 9.	Comparison of the aerosol corrections for the two methods.	15
Figure 10.	The third principal component of the CZCS image shown in Figure 4.	17
Figure 11.	The second and fourth principal components of the image shown in Figure 4.	18
Figure 12.	Grand Banks experiment study area.	20
Figure 13.	Samples of satellite infrared imagery for the Grand Banks experiment area for the period January 1975-October 1979.	21
Figure 14.	Vertical analysis of data from XBTs.	22
Figure 15.	Case I Grand Banks CZCS image formed from channels 1, 2, 3 data uncorrected for atmospheric effects.	24
Figure 16.	CZCS channel 6 (thermal IR) image corresponding to Figure 15.	25

Figure 17. Atmospherically corrected version of Figure 15.	27
Figure 18. NOAA-NESS Gulf Stream Analysis chart for the period 16-20 June 1979.	26
Figure 19. TIROS-N thermal-IR ($11.0\ \mu$) imagery of the Gulf of Mexico on 19 June 1979.	29
Figure 20. CZCS image formed from bands 1, 2, and 3.	32
Figure 21. First principal component of the Case II CZCS image shown in Figure 20.	33
Figure 22. The third principal component of the CZCS image shown in Figure 20.	33
Figure 23. Atmospherically corrected (PCA method) version of Figure 20.	35
Figure 24. XBT data shown as contours of temperature as a function of position and depth.	37
Figure 25. CZCS channel 6 (thermal IR) from orbit 545 over the Gulf of Mexico.	38
Figure 26. CZCS image formed from bands 1, 2, and 3.	39
Figure 27. The first principal component of the Case III CZCS image.	42
Figure 28. Color image formed from the second, third, and fourth principal components of the Case III CZCS image.	43
Figure 29. NOAA-7 infrared imagery for the early morning of 11 October through the afternoon of 13 October.	45
Figure 30. The short term movement of feature shown by Nimbus CZCS and NOAA-7 AVHRR-IR imagery.	48
Figure 31. CZCS image formed from bands 1, 2, and 3.	49
Figure 32. First principal component of the Case IV CZCS image shown in Figure 31.	51
Figure 33. Atmospherically corrected (PCA method) version of Figure 31.	54

Figure 34. NOAA-7 thermal IR (11.0 μ) imagery of the Alboran Sea on 12 October 1982.	55
Figure 35. The second principal component for the Case IV CZCS image.	56
Figure 36. The third principal component for the Case IV CZCS image.	57
Figure 37. Color image formed from CZCS bands 1, 2, and 3 on 30 November 1981.	59
Figure 38. Image formed from application of the universal deep-water algorithm to the image of Figure 37.	61
Figure 39. Image formed from application of the universal shelf-water algorithm to the image of Figure 37.	63

The Use of Principal Components Analysis Techniques on Nimbus-7 Coastal Zone Color Scanner Data to Define Mesoscale Ocean Features through a Warm, Humid Atmosphere

1. Introduction

Oceanographers utilizing satellite data to study ocean mesoscale processes frequently use infrared (IR) sensors that operate in the 8,000-13,000 nanometer (nm) range to produce imagery of the radiation temperatures of the ocean surface (Fig. 1). Unfortunately, these thermal images do not represent exact sea surface temperatures because the data include, in addition to ocean radiation, the absorption and radiation effects of the intervening atmosphere. The atmospheric constituent that contributes the most to corrupting ocean radiation at infrared wavelengths is water vapor. For a cool, dry atmosphere, the effects due to water vapor are sufficiently small so that sea surface temperature patterns are readily observed in IR imagery. In these cases, descriptive analyses may be performed without the need for water vapor correction. However, as the amount and temperature of the atmospheric water vapor increases, the ocean thermal patterns in the imagery become increasingly obscure. Figure 2, a summer image of the Gulf of Mexico, is a good example of the ocean viewed by an IR sensor through a humid atmosphere. This figure may be compared with the winter IR image of the Gulf in Figure 1 to show the lack of observable ocean thermal expression during the summer months.

A graphic demonstration of the effects of the atmosphere in infrared imagery is shown in Figure 3. This NOAA-7 Advanced Very High Resolution Radiometer (AVHRR) image shows a strong atmospheric water vapor front present over the Gulf of Mexico on 19 June 1979. The image shows

more oceanographic details on the dry air side of the front (i.e., in the northeastern Gulf) than in the more humid southwestern side.

The interference of the humid atmosphere, such as that shown in these figures, generally renders satellite infrared sensing of the ocean useless over the tropical oceans during all seasons, and of limited value at middle latitudes over significant portions of the year.

Visible and near-infrared portions of the electromagnetic spectrum are not as severely contaminated by atmospheric water vapor effects as are infrared wavelengths (aerosols are the major problem at visible wavelengths). Therefore, multi-channel visible and near-infrared spectrometers such as the Nimbus-7 Coastal Zone Color Scanner (CZCS) offer the possibility of imaging ocean features through warm, humid atmospheres and may, therefore, open the tropical and summer mid-latitude oceans to studies using satellite remote sensing techniques.

The Nimbus-7 CZCS is a six-channel scanning radiometer. These channels measure the earth's radiance in spectral bands centered at 443 nm, 520 nm, 550 nm, 670 nm, 750 nm, and 11,500 nm. The first four channels are in the visible, the fifth is in the near (reflective) infrared, and the sixth is in the thermal (emissive) infrared portions of the electromagnetic spectrum. Further details on the sensor may be obtained from Hovis et al. (1980).

There are three major questions that must be answered to determine if this



Figure 1. NOAA-7 thermal-IR (11.0μ) image of the Gulf of Mexico for 10 December 1981. The image clearly shows the warm (dark shades) Loop Current flowing into the Gulf through the Yucatan Straits and the seasonally cooled light shades shelf waters adjacent to the landmasses, especially Florida. This image is typical of IR remote sensing through a cool, dry atmosphere.

potential of Nimbus-7 CZCS imagery can be realized for naval operational use:

1) Can ocean color features be imaged from space using the CZCS through the backscattered radiance of the earth's atmosphere?

2) Are the ocean color features seen in the CZCS imagery associated with meso-scale oceanic structures such as fronts and eddies?

3) If ocean color features can be imaged using CZCS data, and they do represent ocean structure, can a routine imaging method be derived that is suitable for Navy use?

An example for the rationale for Question 1 is illustrated in Figure 4. This raw CZCS image of the Grand Banks region of the North Atlantic does not show any major surface structure in this oceanographically dynamical area. Any variability in water color in the data is evidently so subtle as to be completely masked by the atmospheric path radiance. Atmospheric path radiance refers to the sunlight reflected to the satellite from constituents in the air between the satellite and the ocean. Normally more than 90% of the radiance observed from satellite altitudes over the ocean is due to atmospheric path radiance. Thus, to achieve reasonable measurements of ocean radiance, it is necessary to remove this effect.

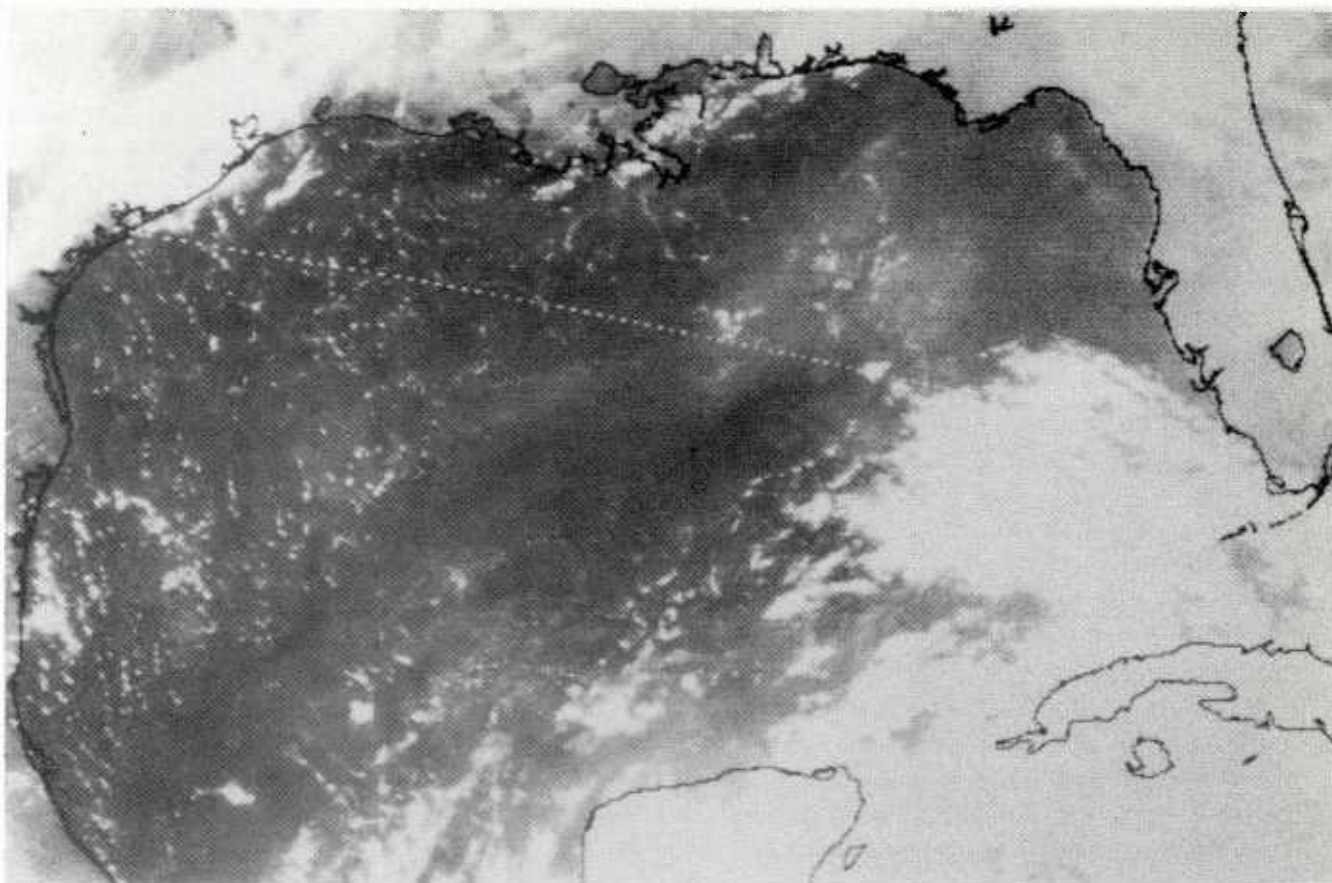


Figure 2. TIROS-N thermal-IR (11.0μ) image of the Gulf of Mexico for 24 June 1979. Note that there is no discernible evidence of the Loop Current or other oceanographic features. This image is typical of IR remote sensing through a warm, humid atmosphere.

The most widely accepted method for correcting for atmospheric path radiance in CZCS data utilizes a model based on single-scattering theory (Gordon, 1978). The single-scattering model requires several assumptions about both the scattering and absorption properties of the atmosphere and ocean. Although these assumptions are valid in many cases, their use in correcting CZCS data can lead to significant uncertainties in other cases.

This report will demonstrate some of the problems and uncertainties encountered in applying the Gordon atmospheric correction and will present an alternative correction method. The method--Principal

Components Analysis (PCA), a statistical tool widely used in the field of pattern recognition--avoids many of the problems associated with the single-scattering model approach. However, it should be noted that at the stage of development presented here, the PCA method does not result in radiance values but generates an atmospherically corrected image in an abstract mathematical space. For this reason the PCA method is not useful where absolute spectral radiance values are required. Thus, it is not presented as a replacement for the single-scattering model methodology; rather, PCA is useful in operationally producing CZCS imagery of ocean features of a quality that allows full descriptive interpretation.

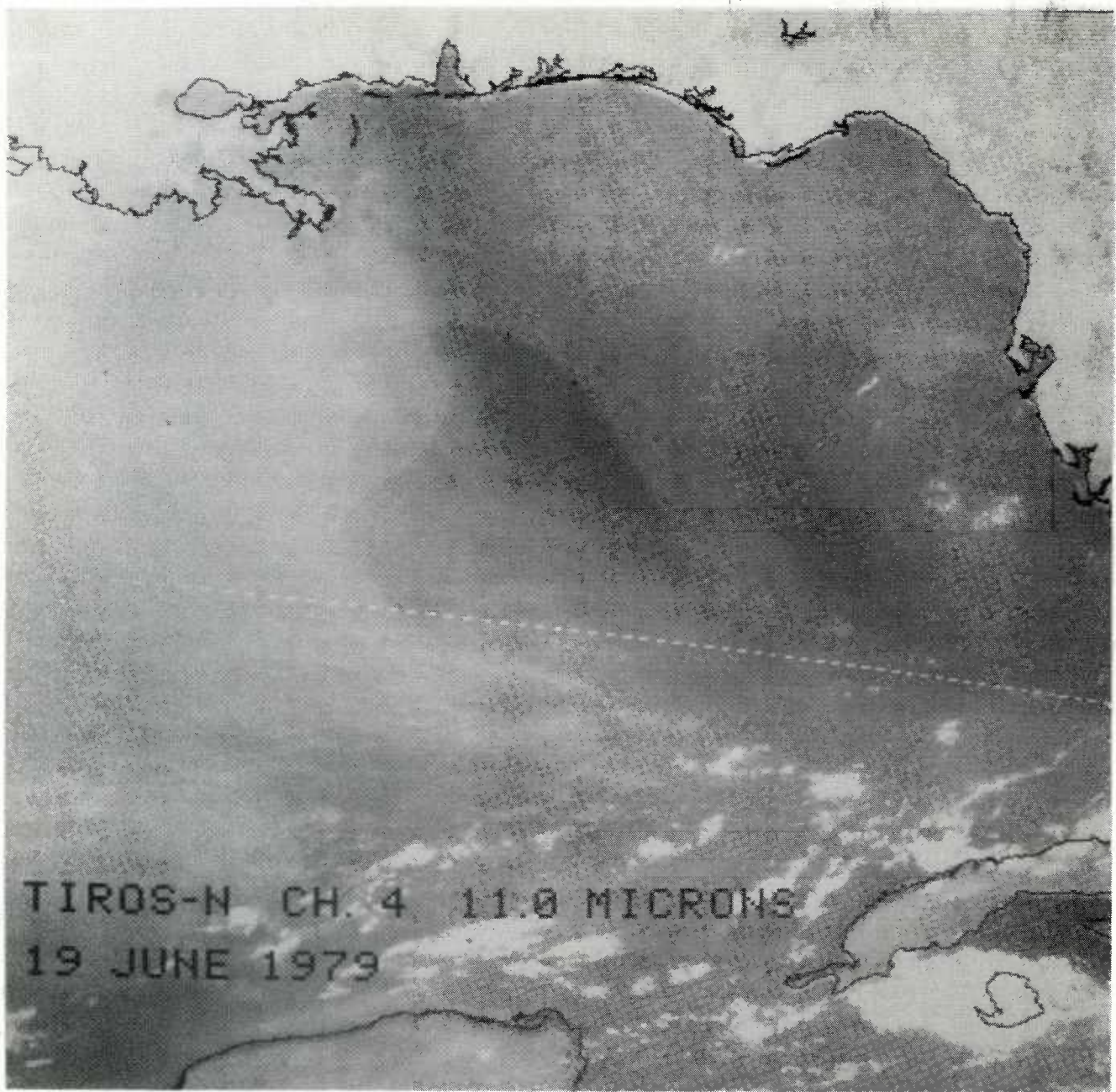


Figure 3. TIROS-N thermal-IR ($11.0\ \mu$) imagery of the Gulf of Mexico on 19 June 1979 showing an atmospheric temperature/humidity front. Note the "clean" appearance of the northeastern Gulf compared with the "foggy" appearance of the south-west quadrant of the figure. The boundary between the two atmospheric regimes is quite sharp and splits the Loop Current in half.



Figure 4. Color image formed from CZCS channels 1, 2, and 3 of orbit 2811 on 15 May 1979 at 1456 Z. Image is from raw data with no enhancements applied. Box outlines the area used for PCA.

2. Atmospheric Correction Techniques: The Single-Scattering Method

The following overview of the CZCS atmospheric correction problem will help identify some of the sources of uncertainty in the single-scattering model methodology.

2.1 The Single-Scattering Approximation

Single-scattering theory, as the name implies, ignores multiple scattering. The theory assumes that a photon traveling the atmospheric path from space to the earth's surface is unperturbed or experiences, at most, one interaction with an atmospheric constituent. This theory is reasonable for optically thin atmospheres but begins to break down for atmospheres that are more optically dense. The advantage of single-scattering theory is that the Rayleigh (molecular) and aerosol (particulate) radiance contributions to the backscattered radiance of the atmosphere are additive. Thus, the observed radiance of the ocean (and atmosphere) as viewed from space is given by

$$L(\lambda) = L_r(\lambda) + L_a(\lambda) + t(\lambda)L_w(\lambda) \quad (1)$$

where $L(\lambda)$, $L_r(\lambda)$, $L_a(\lambda)$, and $L_w(\lambda)$ are the observed, Rayleigh, aerosol, and ocean radiances respectively at wavelength λ , and $t(\lambda)$ is the transmittance of the atmosphere. In Eq. (1), $L(\lambda)$ is observed by the CZCS radiometer and $L_r(\lambda)$ can be calculated with reasonable accuracy (Frohlich and Shaw, 1980). However, $L_w(\lambda)$ and $L_a(\lambda)$ are inseparable, so a direct determination of $t(\lambda)L_w(\lambda)$ is not possible.

To solve for $L_w(\lambda)$, Gordon (1978) uses two wavelengths simultaneously. Taking two equations like Eq. (1), one at λ_2 , and the other at λ_1 , the solution of simultaneous equations yields

$$t(\lambda_1)L_w(\lambda_1) = [L(\lambda_1) - L_r(\lambda_1) - S(\lambda_1, \lambda_2) \{ L(\lambda_2) - L_r(\lambda_2) - t(\lambda_2)L_w(\lambda_2) \}] \quad (2)$$

where $S(\lambda_1, \lambda_2) = L_a(\lambda_1)/L_a(\lambda_2)$.

Gordon (1981) gives the following expression for $S(\lambda_1, \lambda_2)$.

$$S(\lambda_1, \lambda_2) = C(\lambda_1, \lambda_2) [F_o(\lambda_1)/F_o(\lambda_2)] \exp \left\{ - [\tau_o(\lambda_1) - \tau_o(\lambda_2)] [1/\mu_o + 1/\mu_s] \right\} \quad (3)$$

where $\tau_o(\lambda)$ is the ozone optical thickness, $F_o(\lambda)$ is the extraterrestrial solar irradiance, μ_o and μ_s are the cosines of the viewing angle and solar zenith angle respectively, and $e(\lambda_1, \lambda_2)$ is related to the aerosol optical thickness $\tau_a(\lambda)$ and the single-scattering albedo w_o through

$$e(\lambda_1, \lambda_2) = w_o(\lambda_1)\tau_a(\lambda_1)/w_o(\lambda_2)\tau_a(\lambda_2). \quad (4)$$

To solve Eq. (2) for $t(\lambda_1)L_w(\lambda_1)$, one must make assumptions concerning $L_w(\lambda_2)$ and $e(\lambda_1, \lambda_2)$.

2.2 Assumptions About Oceanic Spectral Radiance

The term in Eq. (2) for water radiance at λ_2 , $L_w(\lambda_2)$, is handled by selecting λ_2 such that $L_w(\lambda_2) = 0$; thus, this term can be ignored. For CZCS data the red channel (670 nm) is used as λ_2 . This channel is chosen because the absorption coefficient of sea water is higher at

this wavelength than at wavelengths sensed by the other CZCS visible channels. Thus, relatively small backscatter from the ocean can be expected. Figure 5 shows upwelled spectral radiance data measured just above the ocean surface at several stations in the Gulf of Mexico during December 1978. The data shows that the amount of upwelled radiance does fall off drastically at red wavelengths (actually, most of the observed radiance at 670 nm seen in the Figure 5 data is skylight reflecting off the sea surface rather than subsurface backscatter). Thus, the assumption that ocean radiance in CZCS channel 4 is negligible seems to be reasonable for the deep ocean (i.e., low turbidity) cases. However, this assumption is not valid for coastal regions where significant backscatter does occur at 670 nm. For example, Neville et al. (1980), reporting on

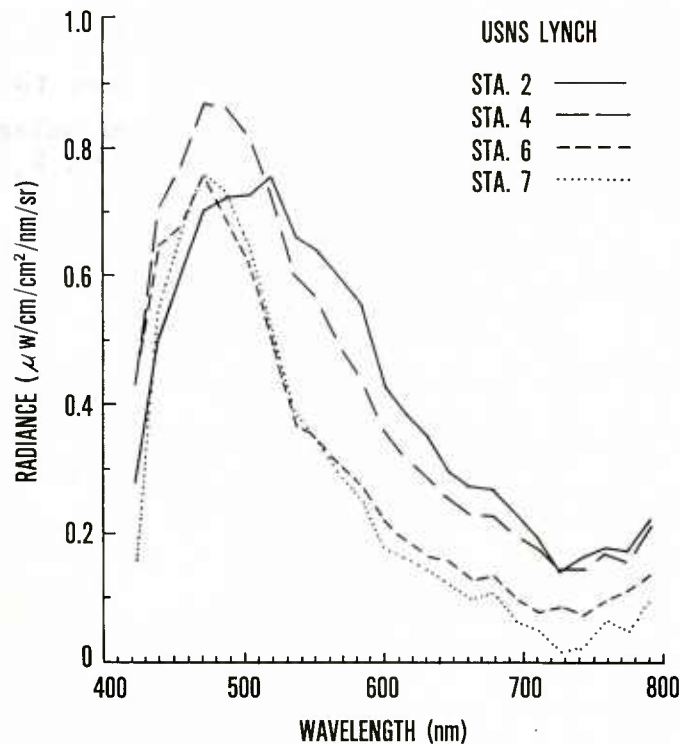


Figure 5. Spectral radiance of the ocean measured from just above the sea surface at several locations in the Gulf of Mexico during November and December 1978.

a study of CZCS data for Lake Ontario, cite appreciable reflectance at 670 nm as the reason for the poor performance of the single-scatter method in their study. To help offset this problem, an iterative algorithm has been developed by Smith and Wilson (1980).

2.3 Assumptions About Uncertainty in Spectral Distribution of Aerosol Backscatter

The factor $e(\lambda_1, \lambda_2)$ in Eq. (5) represents the spectral variability in the aerosol phase function. However, information on atmospheric aerosol phase functions is sparse. For simplicity it can be assumed that the aerosol optical thickness $\tau_a(\lambda)$, varies with wavelength according to the power law

$$\tau_a(\lambda) = \tau_a(\lambda_0)(\lambda_0/\lambda)^n \quad (5)$$

where n is referred to as the Angstrom exponent (Angstrom, 1961).

To make an atmospheric correction to CZCS data, one must either measure n at the time of satellite overpass or assume a value for n . Gordon (1978) assumes that the aerosol phase function depends weakly on wavelength over the visible part of the spectrum, i.e., that the value of n is approximately zero. However, this is not strictly true in all cases and the Angstrom exponent for atmospheric aerosols has been found to range between 0 and 2 (Robinson, 1966). Tomasi and Prodi (1982) in measuring atmospheric turbidity in the Red Sea, Indian Ocean, and Somalian Coast found n values that ranged between 0.2 and 0.9.

Measurements of the aerosol optical depth of the atmosphere made in November and December 1978 in the Gulf of Mexico are shown in Figure 6, along with power law fits of the measured values. The figure shows that the power law fit to aerosol optical depth is only approximate and that the Angstrom exponent actually varied from day to day; ranging

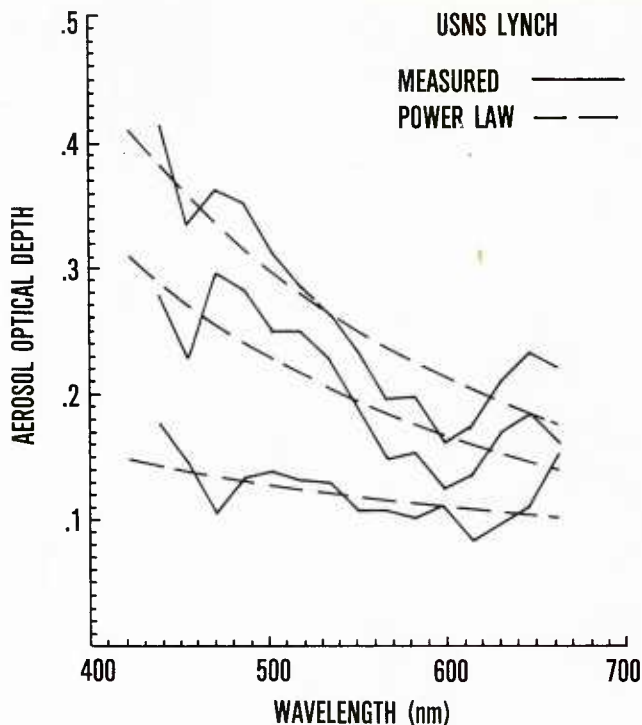


Figure 6. Aerosol optical depth of a vertical atmospheric path measured in the Gulf of Mexico onboard the USNS LYNCH on three different days in December 1978. Dotted lines are power law fits to the measured data.

from 0 to 1.9 with a mean value of 1.2. This mean is close to the 1.3 value often used for continental regions (Robinson, 1966). Because of this type of aerosol variability, large errors in correction terms can result when 670 nm values are extrapolated into the green and blue regions based on some assumed value for n .

Gordon and Clark (1981) propose using spectral radiance values from a clear water portion of a CZCS image to derive values for the Angstrom exponent. They state that good results are possible if a water area with less than 0.25 mg/m^3 of chlorophyll-a can be found within a given scene.

The single-scatter modeling approach to atmospheric correction may, therefore,

be summarized as follows: Each of the four CZCS channels are corrected for the Rayleigh backscatter of the atmosphere. Since the ocean is assumed to be "black" at 670 nm, any radiance remaining in channel 4 after the Rayleigh correction is attributed to atmospheric aerosols. The Rayleigh-corrected red (670 nm) channel is, therefore, the aerosol correction term that is applied to the remaining three channels. However, before application, the correction term is differentially weighted for each of the three channels. The weighting factors are somewhat subjective and require knowledge of the solar spectral irradiance, the ozone optical depth, and the Angstrom exponent for the atmospheric aerosols for each case.

Thus, the corrected CZCS image may differ significantly from the actual ocean spectral radiance for three important reasons:

- the single-scattering approximation may be poor because the atmosphere is optically thick;
- the ocean is not really "black" at 670 nm;
- an incorrect value has been used for the Angstrom exponent.

2.4 The Single-Scattering Model Applied to a Test Case

A simplified form of the single-scattering model applied to an ocean data set will both illustrate the essential elements of this established method and serve as a reference for evaluating the proposed statistical method. The data used is from the Grand Banks CZCS image shown in Figure 4. The CZCS thermal infrared image (channel 6) corresponding to the CZCS visible data is shown in Figure 7. This area, one of the most dynamic regions in the oceans, forms the confluence of three major current systems: the Gulf Stream, the Labrador Current, and the North Atlantic

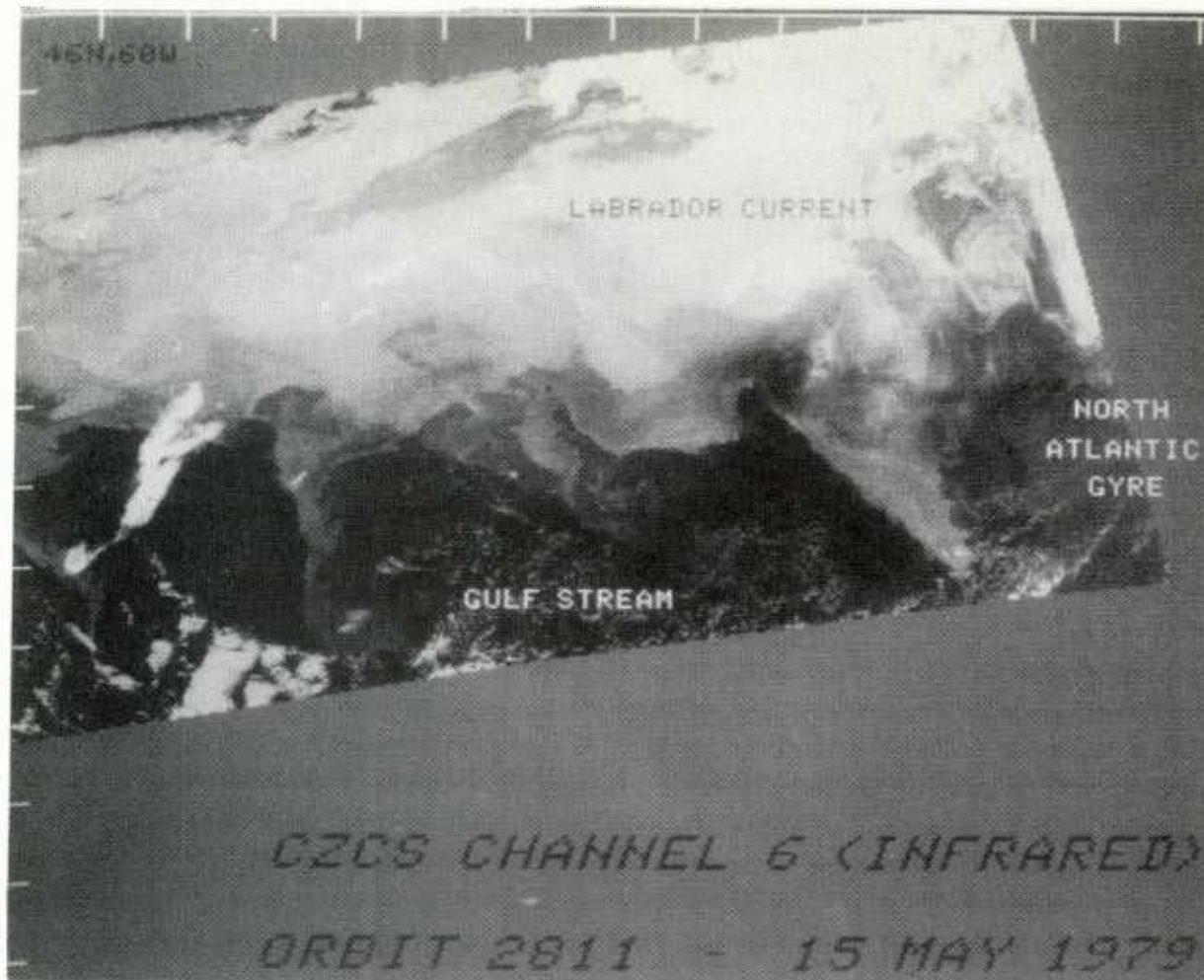


Figure 7. Image of CZCS channel 6 (infrared) data coincident with Figure 4. Labels on image identify major oceanographic regimes.

Current. Note that although the surface thermal gradients created by the encounter of the thermally different currents are well-delineated in the IR imagery, no corresponding features are discernible in the visible color image. Either there is no color signature associated with these divergent current systems, or the ocean surface upwelling radiance is obscured by the more dominant atmospheric backscatter. The data, therefore, present an ideal case to demonstrate the two atmospheric correction procedures.

The single-scattering model atmospheric correction was performed on the data following the general methodology previously described. Clear water radiances

(Gordon and Clark, 1981) were used to derive an Angstrom exponent of 2.8 for this case. Solar irradiance values, F_0 (λ), were assumed to be 184.63, 185.57, 185.01, and 153.13 in CZCS channels 1, 2, 3, and 4, respectively (Austin, 1981). The values for ozone transmittance of the atmosphere, $\tau_o(\lambda)$, were taken to be 0.0009, 0.0146, 0.0266, and 0.0138 from the LOWTRAN-5A code (Kneizys et al., 1980) for a mid-latitude summer atmosphere. Solar and satellite zenith angles were held constant at their values in the box drawn in Figure 4. Solar and satellite zenith angles at that location are 23.5° and 25°. Not



Figure 8. Color image formed from atmospherically corrected CZCS channels 1, 2, and 3. Atmospheric correction was by means of a simplified single-scattering atmospheric model.

permitting these angles to vary spatially results in Rayleigh correction errors of 15% at the left edge of the image in the figure and 25% at the right edge. (The limb effects seen in the corrected data would largely disappear if angular dependence was included in the Rayleigh processing.)

When the single-scattering correction is applied, the corrected radiance values in channel 1 (443 nm) become negative. Since this is physically impossible, it implies that the correction method, or at least the values of the method parameters, is erroneous. Negative corrected radiances could result from several sources including uncertainties in solar spectral irradiance or sensor calibration. In this case the Angstrom exponent value of 2.8, derived from clear water radiances, seems suspiciously large (since the Angstrom exponent is generally considered to range from 0 to 2). There is no obvious explanation why the clear water radiances gave such a large value, nor is there ground truth or other collaborating data. Prelaunch calibration data are used to convert raw data to radiance values. The prelaunch and in-flight calibration to CZCS is presently a matter of considerable uncertainty. It could be that poor calibration data led to the large n value. If the clear water radiance approach is abandoned and a mid-range Angstrom exponent of 1 is assumed, the following values $S(\lambda_1, \lambda_2)$ result:

- $S(443, 670) = 1.80$;
- $S(520, 670) = 1.56$;
- $S(550, 670) = 1.44$.

The atmospheric correction of the CZCS image is repeated using these values. The channel 1 radiances now come out positive. A subjective visual examination of the corrected imagery indicates that a reasonable correction of the data has been made.

Figure 8 is a color composite of the three channels of atmospherically corrected data that shows an ocean different than that shown in the CZCS image of

Figure 4. The correction appears to have effectively stripped away the atmospheric path radiance revealing oceanic color patterns similar to the general features in the thermal image of Figure 7.

3. Atmospheric Correction Techniques: Principal Components Analysis Method

To overcome some of the single-scatter method problems in the case just described, the atmospheric correction of CZCS imagery can be approached as a statistics problem. With this approach, assumptions about physical properties that are part of the Gordon (1978) method, such as that the ocean is black at 670 nm, or that the aerosol phase functions vary only weakly with wavelength, are replaced with assumptions about the statistical properties of the data. With this method an assumption is made that there is an area of the image where most of the variance in the multi-spectral measurement space is attributable to aerosol variability. Two important criteria of the area where this statistical property exists are: 1) the area should have a high variability in aerosol concentration, and 2) the ocean be nearly uniform in color. For this reason coastal waters, with their typically high water color variability, are avoided. Likewise, areas with clouds are avoided since the brightness of a cloud would saturate the eight-bit dynamic range of the CZCS. Such saturation introduces a nonlinearity into what is basically a linear transformation technique.

3.1 Principal Components Analysis

Principal Components Analysis (PCA) is most frequently used in pattern recognition problems to reduce the dimensionality of a measurement space. For example, it is possible to transform 10-channel multispectral imagery into only three channels, and yet preserve 95% or more of the "information" present in the original 10-channel data. In PCA "information" is synonymous with variance; i.e., PCA is a dimensionality reduction tool that preserves the maximum possible

variance. In some situations, the variance present may be due to noise rather than information, so an analyst should know the statistical properties of the data before choosing to use PCA. In the present case, the image subarea selected for PCA has been chosen to have the assumed statistical properties. If these desired properties do exist in the data, then the same characteristics of PCA that make it useful for dimensionality reduction make it useful for atmospheric corrections.

From a mathematically nonrigorous point of view, PCA is the linear transformation of a given set of variables to a new set of variables called principal components. This new set of variables is arranged in a sequence such that each succeeding component is that linear combination of the original variables which has the maximum variance of all possible combinations under the constraint that each component be uncorrelated with, and orthogonal to, all preceding components. (More details may be found in Anderson, 1958, or Cooley and Lohnes, 1971.) It can be shown mathematically that the principal components defined in this manner are, in fact, the eigenvectors of the covariance matrix. Furthermore, it can be shown that the variance of the i -th principal component is identically equal to the i -th eigenvalue of the covariance matrix.

The variance-ordering properties of the principal component sequences and the fact that most of the variance in the selected subarea of the image results from aerosol variability are the basis for the removal of the aerosol effects. If the first principal component maximizes variance, then this component captures the aerosol contribution to the total variance. In other words, because the selected subarea is bland oceanographically, the orientation of the first principal component will be parallel to the aerosol variability. The first principal component can, therefore, be discarded to make the aerosol correction. In the CZCS image used to

illustrate the technique, the original measurement space is four-dimensional (CZCS channels one through four). PCA results in a transformation to a new four-dimensional space. If the first new dimension (or first component) is removed (i.e., projected onto the other three in mathematical terms), the result is a three-channel image, with the obscuring effect of atmospheric aerosols removed. Because of this removal, the resulting three-channel image will show the oceanic portion of the variance that was hidden in the original image.

3.2 Statistics of the Test Case Data

Statistics for the selected subarea in the Grand Banks data set in Figure 4 (boxed in the image) are given (p.16), along with the principal components and the eigenvalues of the covariance matrix. As previously mentioned, the principal components are formed from linear combinations of the original spectral bands. If x_{ij} is the i -th subarea pixel from channel j , then the k -th principal component, P_{ik} , can be written

$$P_{ik} = \sum_j a_{kj} x_{ij} \quad (6)$$

The coefficients a_{kj} , therefore, define the transformation from spectral measurement space to principal component space. The statistics below are given in vector form where the vector components represent each of the four spectral bands. This data has not been radiometrically calibrated, so the values given are in units of raw digital counts.

Note that the eigenvalues indicate that the first principal component (the atmospheric aerosol component) in this case account for 96.6% of the total variance within the box. This means that only 3.4% of the variance is of oceanic origin, which explains why oceanic features could not be seen in the raw data in Figure 4.

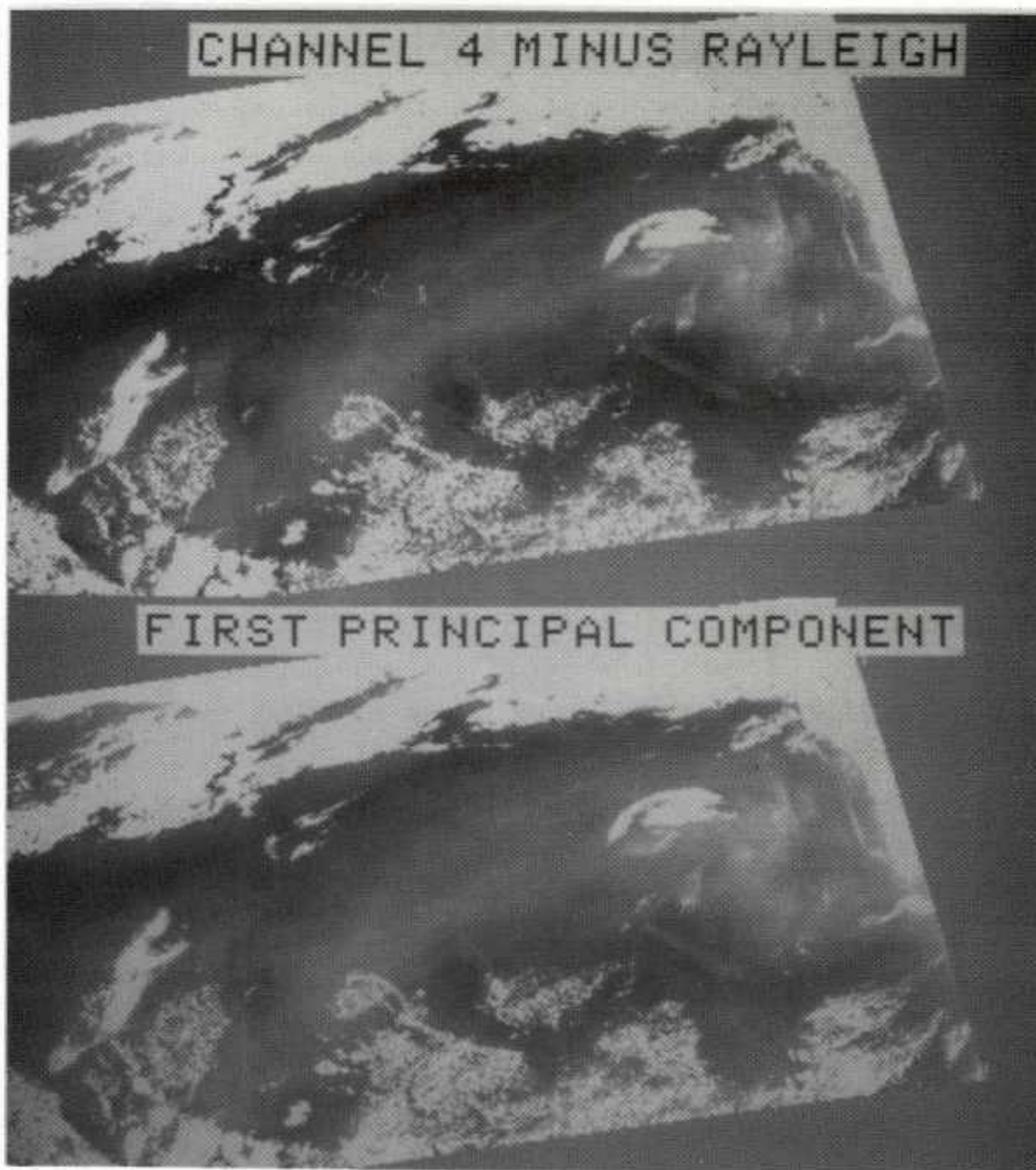


Figure 9. Comparison of the aerosol corrections for the two methods. The upper figure is the aerosol correction from single-scattering theory, and the lower figure is the aerosol correction from the PCA method.

Case I Grand Banks PCA Box Statistics

mean = 162, 149, 151, 148
std dev = 6.57, 8.64, 10.13, 17.08
eigenvalues = 0.966, 0.028, 0.004, 0.001

	0.265	0.381	0.451	0.761
a_{kj} =	-0.731	-0.382	-0.159	0.541
	-0.529	0.199	0.743	-0.356
	0.337	-0.817	0.466	0.015

The a_{kj} values, particularly the weights for the third principal component, are also interesting. The coefficients -0.529, 0.199, and 0.743 for channels 1, 2, and 3, respectively (row 3 of the matrix), indicate that this component shows changes associated with chlorophyll concentrations. This statement is based on the fact that the component is composed of large contributions from channels 1 and 3 that are opposite in sign plus a relatively small contribution from channel 2. This weighting exhibits the well-known "hinge point" signature of chlorophyll-a (Duntley et al., 1974). In a deep ocean location like the Grand Banks, chlorophyll is normally the primary contributor to ocean color, so it would be expected that this third component will probably show more oceanic structure than will the other components.

3.3 Corrected Imagery

The a_{kj} coefficients derived from PCA within the boxed area in Figure 4 can now be used as a transformation matrix to be applied to the entire image according to Eq. (6). If the initial assumptions about the statistical properties of the data are valid, the first principal component, which contains 96.6% of the total variance in the sub-area, can be assumed to represent the path radiance resulting from aerosol backscatter. For a check on this assumption, Figure 9 shows the first principal component and the original channel 4 image with the Rayleigh radiance contribution removed (i.e., the aerosol

correction factor using the single-scattering method). Visual comparison of the two indicates that an aerosol correction based on the first principal component will be very similar to a correction based on Rayleigh corrected channel 4.

As expected, the third principal component shows the most features of apparent oceanographic origin. Figure 10 is an image of the third principal component, which accounted for 0.4% of the total variance. Comparison of Figure 10 with the IR data (Fig. 5) and the color image corrected by the single-scattering method (Fig. 8) reveals that the oceanographic features shown in these earlier figures are also evident in the third principal component image. Thus, the third component is, in effect, an atmospherically corrected image showing ocean color variability patterns. It should be noted that the third component will not always be the component to give maximum definition of oceanic patterns. In other cases where PCA was applied to a small subsection of an image so that angular variation of path radiance was small, the second component seemed to contain the chlorophyll-a variance and, hence, the best oceanic patterns. In general, it cannot be stated which component will best show the ocean patterns.

The second and fourth components contain some oceanographic information but are predominated by other influences. The second component, with 2.8% of the total variance, seems to represent the angular dependence of the atmospheric path radiance, while the fourth, with <0.1% of the total variance, contains mainly random noise. For sake of completeness, components two and four are shown in Figure 11.

3.4 Atmospheric Correction Summary

The Grand Banks data set has been used to show how a statistical approach based



Figure 10. The third principal component of the CZCS image shown in Figure 4.

on PCA can be used to develop CZCS aerosol correction terms that are essentially equivalent to those derived from single-scattering theory. The example shows that the statistical analysis can be performed in a relatively straightforward manner that does not have to consider such problems as the determination of an Angstrom exponent, the validity of ocean blackness at 670 nm, sensor calibration, or many of the other problems associated with using the modeling approach. Further, the example shows that the statistical approach has resulted in an aerosol-corrected image that apparently shows ocean features. It is concluded, therefore, that PCA may be

an easy to use alternative to single-scatter modeling of the atmosphere for those applications where image pattern interpretation, rather than ocean spectral radiance measurement, is the objective. To further show the utility of PCA, four case studies are presented in the following section for three ocean regions.

4. CZCS Case Studies

One of the questions posed in the introduction was, "Do deep ocean fronts typically have color signatures?" As an aid to answering this question, four data sets representative of three different

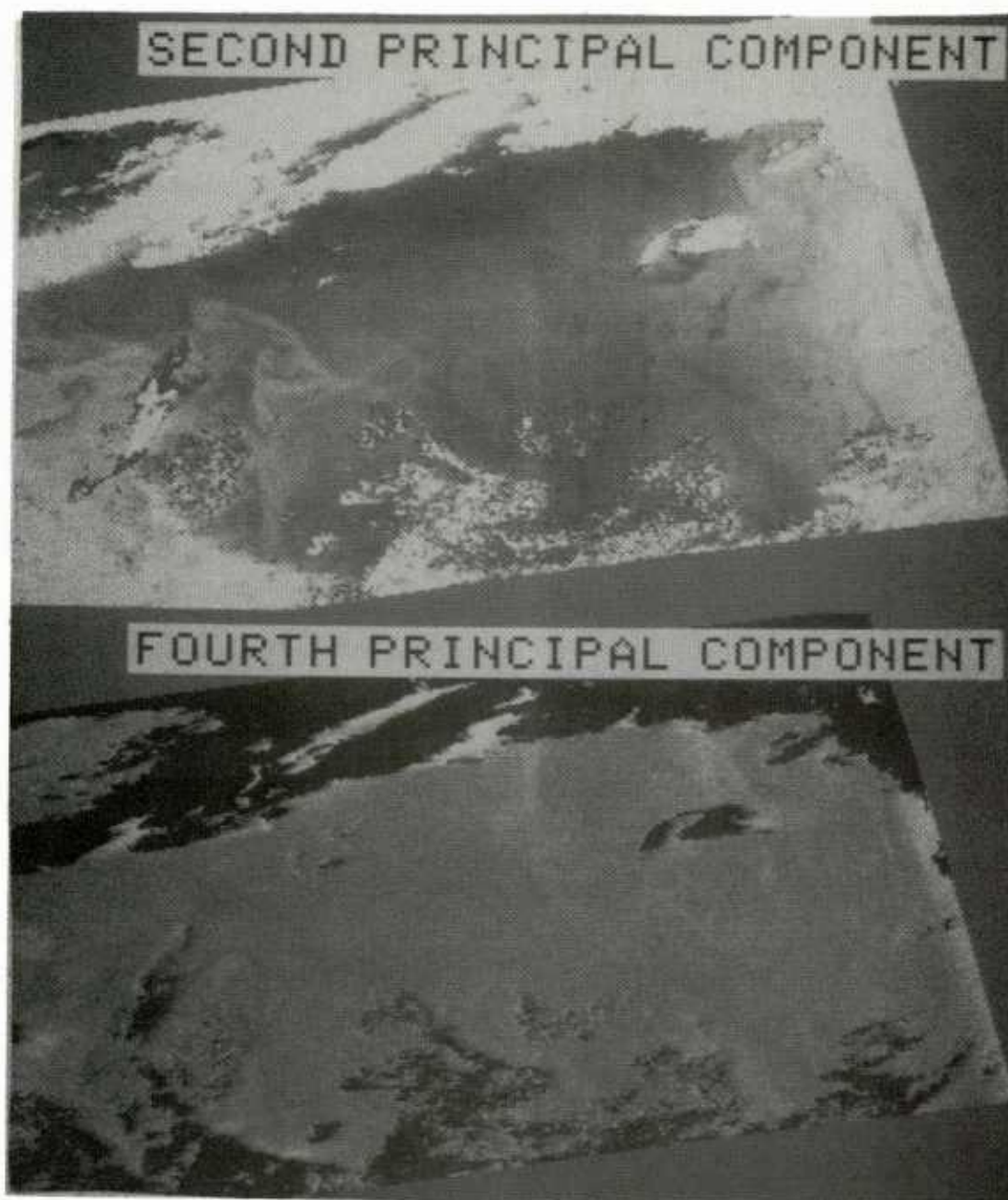


Figure 11. The second and fourth principal components of the image shown in color (Fig. 4) on page 5.

ocean areas have been selected to be atmospherically corrected by the PCA method. These atmospherically corrected images are compared with coincident NOAA-IR imagery and surface data in an attempt to establish the relationship between the patterns found in the PCA corrected CZCS imagery and actual ocean features. The four test cases are:

- Case I. Grand Banks, 15 May 1979;
- Case II. Gulf of Mexico (summer), 19 June 1979;
- Case III. Gulf of Mexico (winter), 6 December 1978;
- Case IV. Mediterranean, 12 October 1982.

4.1 Case I—Grand Banks

The Grand Banks area of the North Atlantic received intensive study during the Grand Banks Experiment in 1978 and 1979 (La Violette, 1981). The Nimbus-7 CZCS image chosen for analysis was acquired on 15 May 1979 during the "New Look" portion of the Grand Banks Experiment. This case is accompanied by extensive surface data.

4.1.1 The Surface Data

The study area for the Grand Banks Experiment is shown in Figure 12. The bathymetric features, such as the Newfoundland Ridge and the Newfoundland Seamounts, are important controls of the currents in the area. A study of satellite imagery for the 5-year period, 1975-1979, showed that the fronts and eddies associated with the interaction of the Gulf Stream, Labrador Current, and North Atlantic Gyre were consistently positioned in the area of the three nodes shown in the simplified schematic in Figure 13 (La Violette, 1981).

As might be expected from the fact that these nodal positions are correlated with the regional bathymetry, the ther-

mal features seen in the satellite imagery are not simply surface effects but are the surface manifestations of dynamic structures that extend to 1000 m in depth. Figure 14 is a temperature cross-section across node 1 derived from a line of Airborne Expendable Bathymographs (AXBT) recorded on 16 May 1979 (the day after the images of Figures 4 and 7 were acquired). This cross section clearly shows that the depth of the structure associated with node 1 extended deeper than the 400-m limit of the AXBTs.

4.1.2 The CZCS Data

The CZCS data set for this case study is the same that was used to demonstrate the atmospheric correction techniques in Section 3. In that case, the image shown covered an east-west swath of approximately 15° of longitude that included nearly the entire CZCS scan width. However, this discussion covers only the eastern half of the image (i.e., the area located over nodal features 1 and 2). Figure 15 is a color image formed from channels 1, 2, and 3 of CZCS orbit 2811 data. The scale of Figure 15 is such that the spatial resolution is about 1.5 km/pixel compared with the 0.8 km/pixel nadir resolution of the original data. The Labrador Front nodal positions are marked for reference purposes, to show that the atmospherically uncorrected data does not reveal the presence of these oceanographic features. Figure 16 is the channel 6 thermal-IR image corresponding to Figure 15. Note the predominance of the two nodal features in the sea surface temperature image.

The CZCS image, atmospherically corrected by means of PCA is shown in Figure 17. Now, oceanographic patterns are displayed that closely resemble those in the infrared image of Figure 16, thus indicating that the currents that give rise to the surface thermal patterns exhibit associated ocean color signatures.

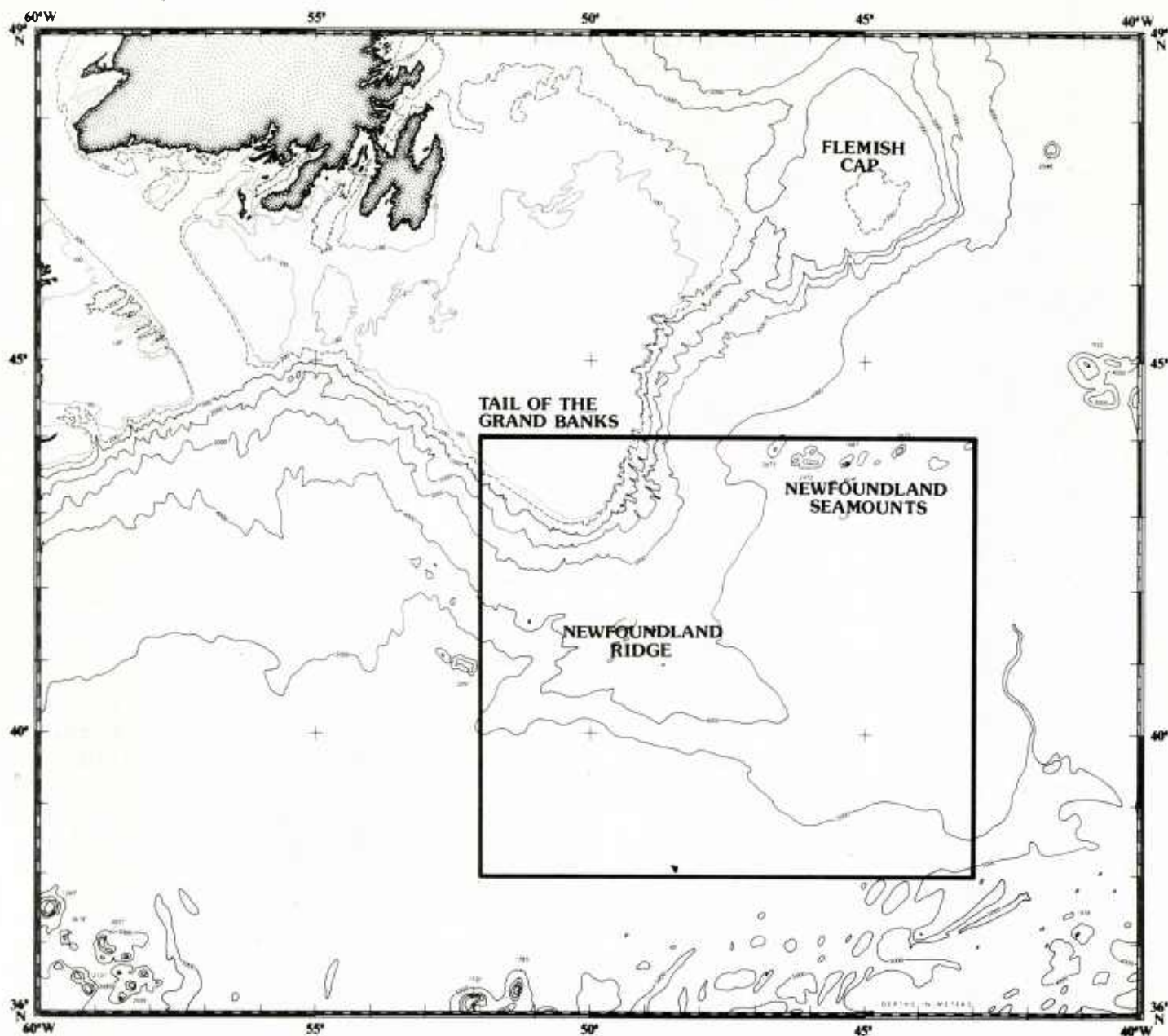


Figure 12. Grand Banks Experiment study area. The square represents the major ship and aircraft survey area (After La Violette, 1982).

4.1.3 Discussion of Case I

Although the general nature of the color and thermal patterns in Figures 16 and 17 are similar, there are noticeable differences that are of oceanographic interest. For example, the IR image shows a single well-defined front on the southwestern side of node 1. In the

color image two fronts are present; one corresponds exactly with the temperature front, and the second lies parallel to the first front but offset to the southwest by 40 to 50 km. The thermal imagery does not indicate a thermal feature at the location of the second color front. Discussion of this particular color/temperature frontal structure has been given by Mueller and La Violette (1980).

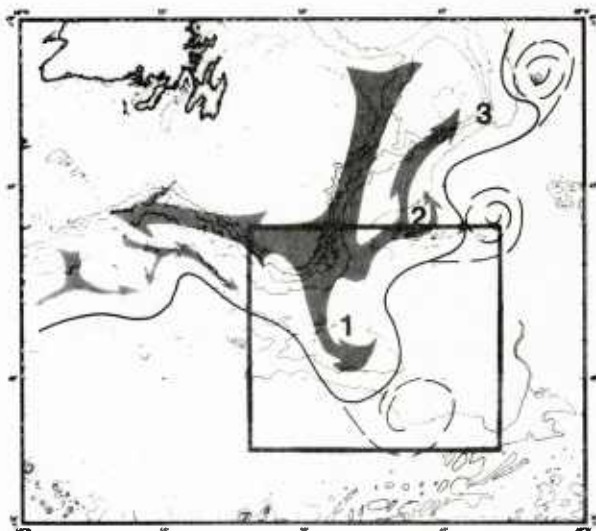
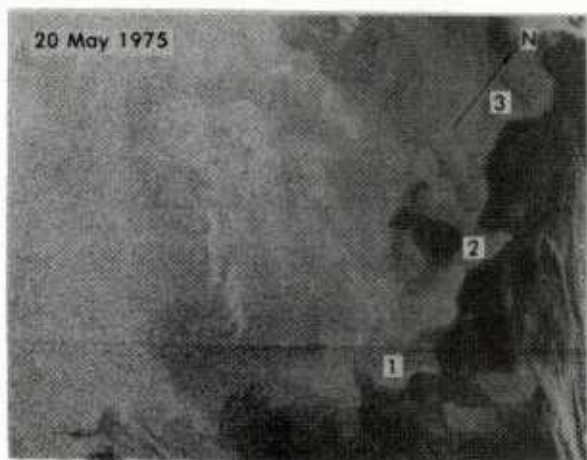


Figure 13. Samples of satellite infrared imagery for the Grand Banks Experiment area for the period January 1975 through October 1979. These imagery show that three frontal extrusions were always present in the cloud-free data. However, imagery showing all three structures at one time are rare. The ones presented here are meant only as examples of these features. Newfoundland is the dark land mass in the upper left corner of each image. The line drawing on the bathymetry chart is a composite of all the imagery for 1978, and is drawn by hand on a common grid. The solid line represents the edge of the cold water of the Labrador Front. The dashed line represents the direction and type of extrusion away from the front. The shaded area northwest of the front represents the dominant position of the Labrador Current as seen in the imagery. The smaller shaded areas in the west are smaller slope water current features that also appeared in the 1978 imagery. Composites drawn from other years' imagery show similar results. (After La Violette, 1982)

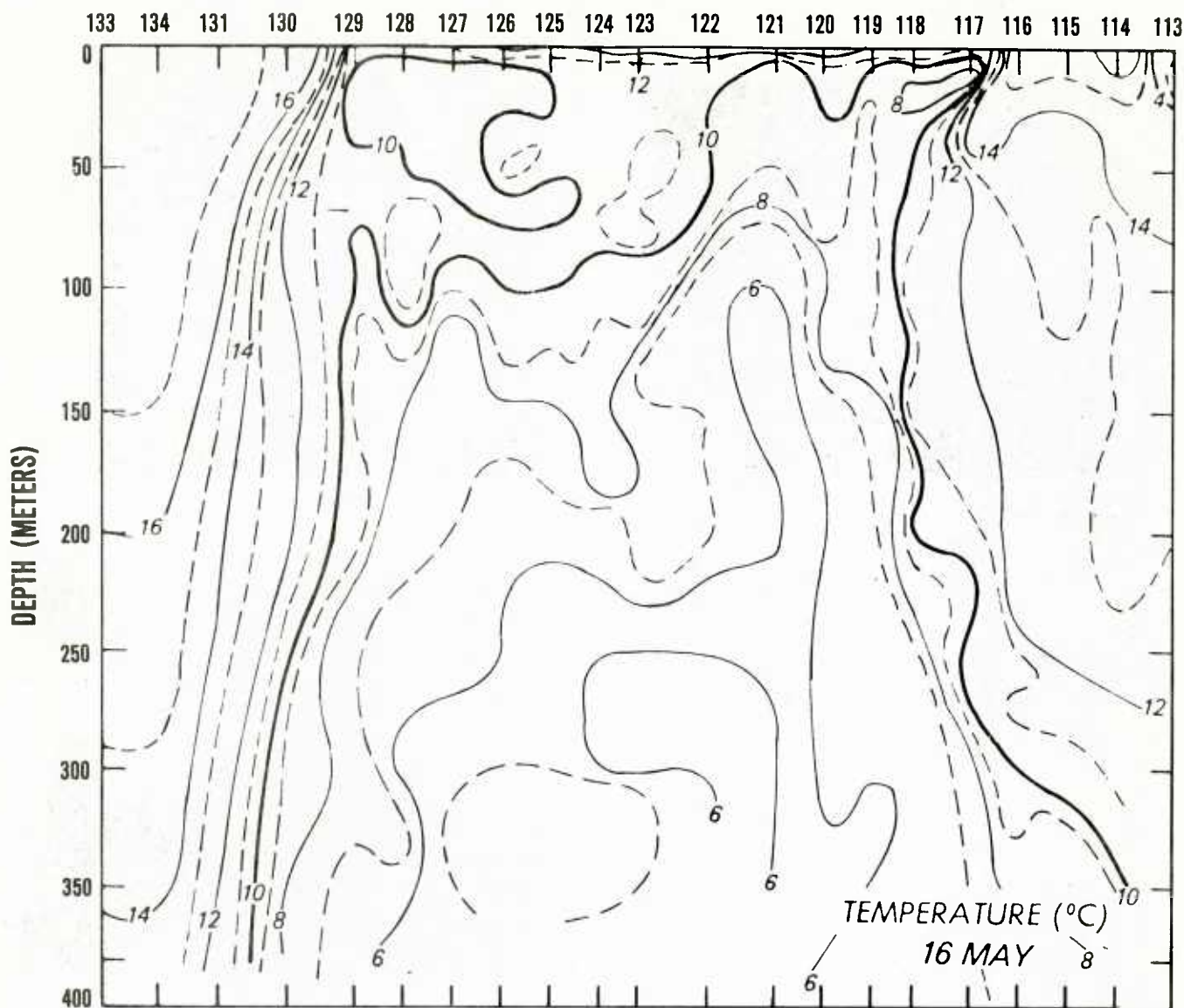


Figure 14. Vertical analysis in $^{\circ}\text{C}$ of data from aircraft XBTs dropped on 16 and 17 June 1979.

The oceanographic interpretation of the ocean color patterns observed in Figure 17 is conjectural. Even with the extensive ground truth available, one cannot really give more than hypothetical explanations for what is observed. However, for the purpose of this study, it is important to state that Figure 17 shows that the interacting current systems in the Grand Banks area do have color signatures discernable in the CZCS data.

4.2 Case II—Gulf of Mexico (Summer)

The second case illustrates the effect of mid-latitude summer atmospheric conditions (19 June 1979) in the CZCS data. This example, although not accompanied by good surface data, is a good one for the purposes of this study. In the image, the unusual late season outbreak of cool, dry continental air over the northeastern Gulf of Mexico permits localized NOAA IR imaging of sea surface

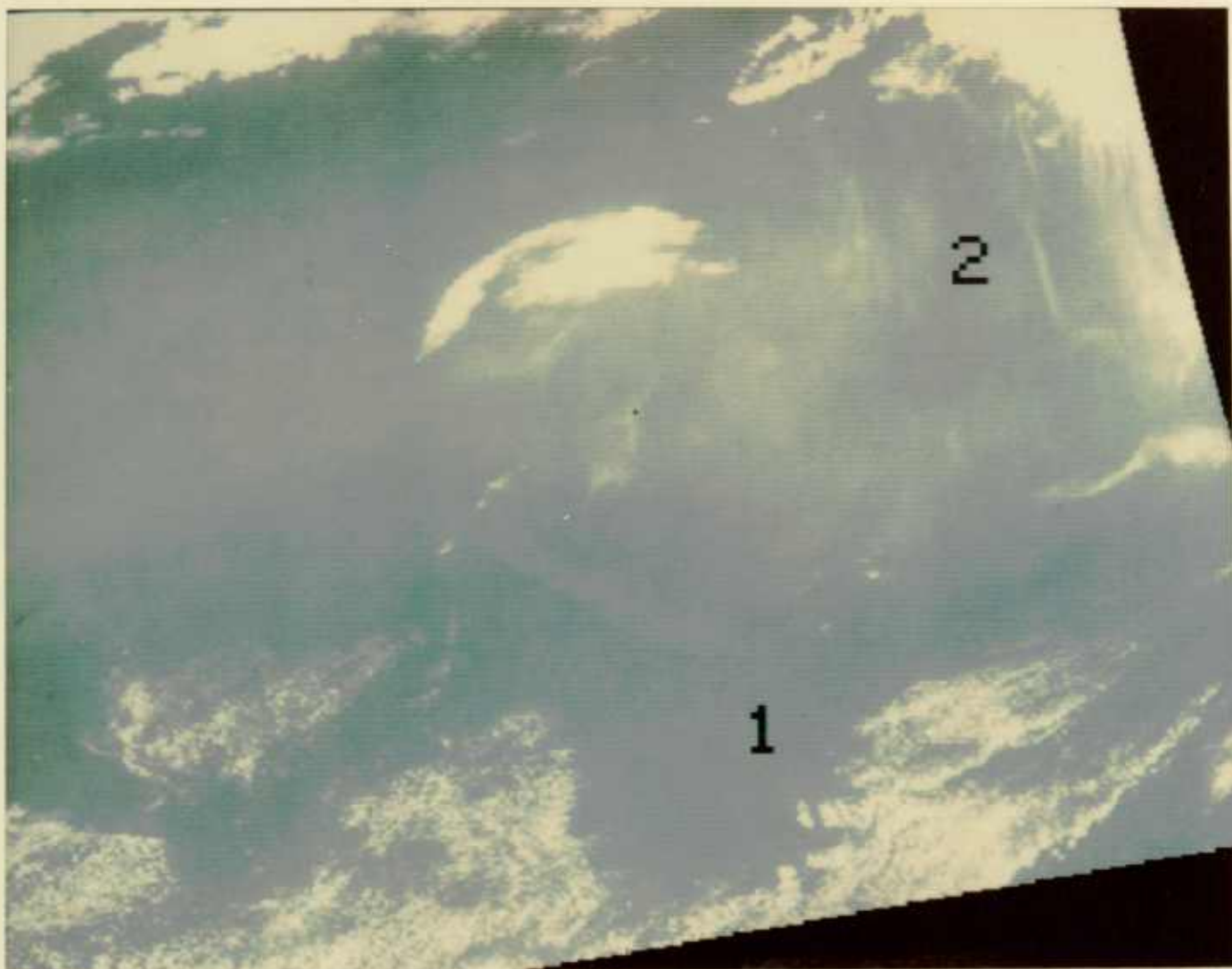


Figure 15. Case I Grand Banks CZCS image formed from channels 1, 2, and 3 data uncorrected for atmospheric effects. Position of nodes 1 and 2 from Figure 13 are marked.

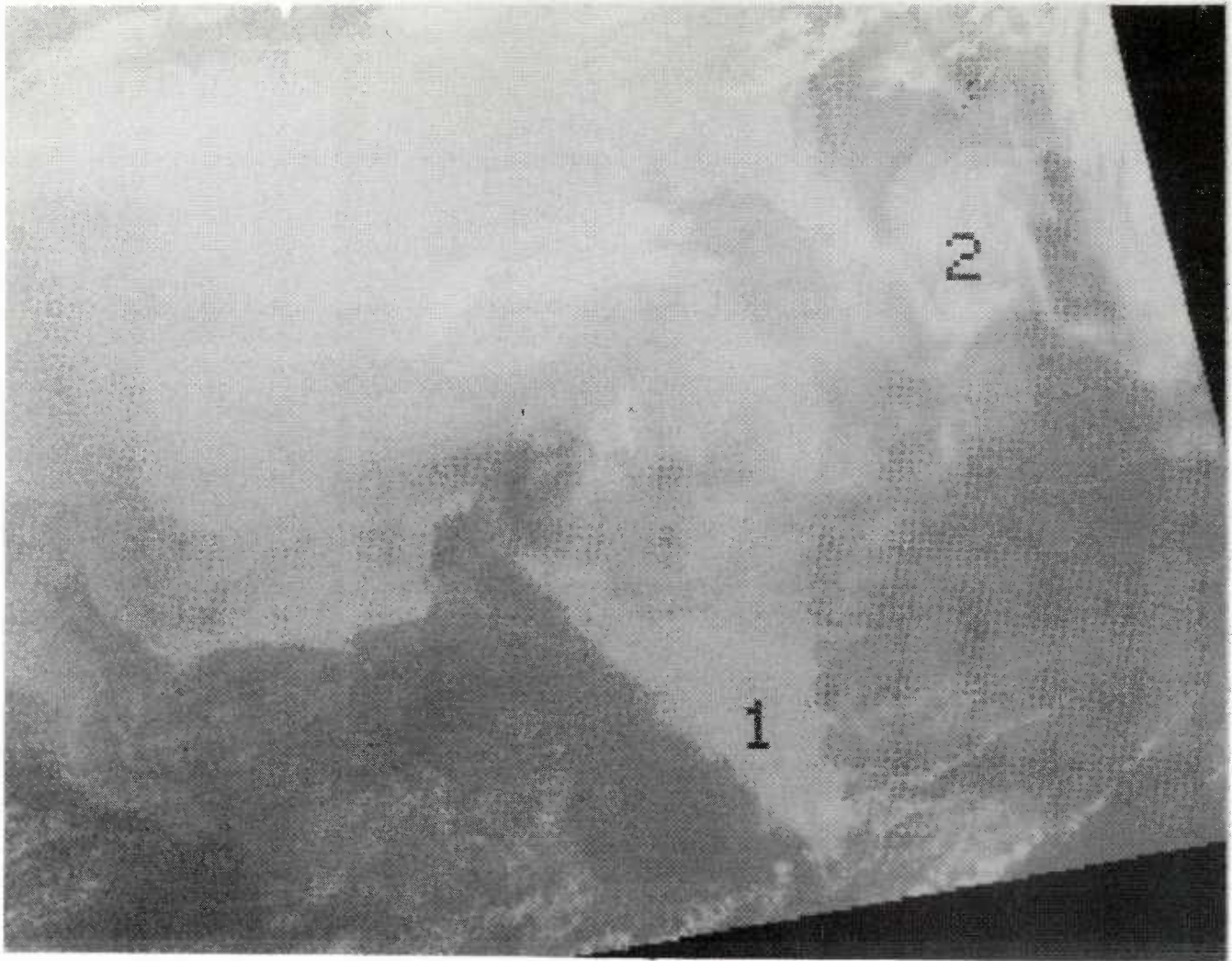


Figure 16. CZCS channel 6 (thermal IR) image corresponding to Figure 15.

thermal patterns that is not normally possible in the Gulf of Mexico in late June because of the seasonal warm, humid atmosphere. The main CZCS verification in this case, then, will be a comparison of the CZCS color patterns and the local mesoscale ocean features seen in the NOAA image. It will also be of interest to see the color patterns discernible in those areas where the warm, humid atmospheric conditions obscure the ocean thermal patterns.

4.2.1 The Surface Data

Although there is no specific surface data to support an analysis of this CZCS

data set, the NOAA-NESS Gulf Stream analysis for 16-20 June 1979 (Fig. 18) does have the Loop Current boundary well-defined. According to NOAA-NESS practice, all available concurrent ship reports, XBTs, or AXBTs available from the Gulf of Mexico commonly are incorporated into their analysis. So, although the accuracy of the NOAA-NESS Loop Current boundary location is not known, it can be assumed that the location plotted on the chart is not in conflict with available surface data.

Figure 19 shows the TIROS-N IR (channel 4) image from orbit 3510 on 19 June 1979 (the figure is an enlargement of a sec-

tion of Fig. 3). Note the effect of the cool, dry air over the northeastern Gulf. Here the position of the Loop Current is clearly visible. The Loop Current, however, fades from view to the south and west under the typical Gulf of Mexico summer atmosphere.

4.2.2 The CZCS Data

Figure 20 is a color image formed from CZCS channels 1, 2, and 3 of Nimbus-7 orbit 3310 on 19 June 1979. (The image has been subsampled to approximately a 3.3 km/pixel spacing to contain the entire Gulf of Mexico.) The wide, bright band, lying in an approximate northwest-southeast orientation of the image, is apparently caused by sun reflecting off the ocean surface. On this particular orbit, the CZCS was tilted to look behind the spacecraft at a 20° tilt angle. Thus, for this ascending trajectory, the scanner was oriented toward the south where it received the sea's reflection

of the sun at its near-zenith summer time position. Because of the presence of this sun glint, the image is uncorrectable by the single-scattering model. The example is of additional interest as it demonstrates the advantage of the PCA atmospheric correction method for images contaminated by sun glint.

The image subarea chosen for PCA purposes is enclosed in the box superimposed on the image in Figure 20. Statistics of the data within the box are shown below.

Case II Gulf of Mexico PCA Box Statistics

mean = 193.1, 188.9, 198.9, 238.6
std dev = 3.74, 3.80, 4.70, 7.12
eigenvalues = 0.581, 0.338, 0.075, 0.003

$a_{kj} = \begin{matrix} & 0.045 & 0.229 & 0.341 & 0.910 \\ -0.517 & -0.574 & -0.517 & 0.365 \\ -0.849 & 0.284 & 0.405 & -0.181 \\ 0.090 & -0.731 & 0.671 & -0.072 \end{matrix}$

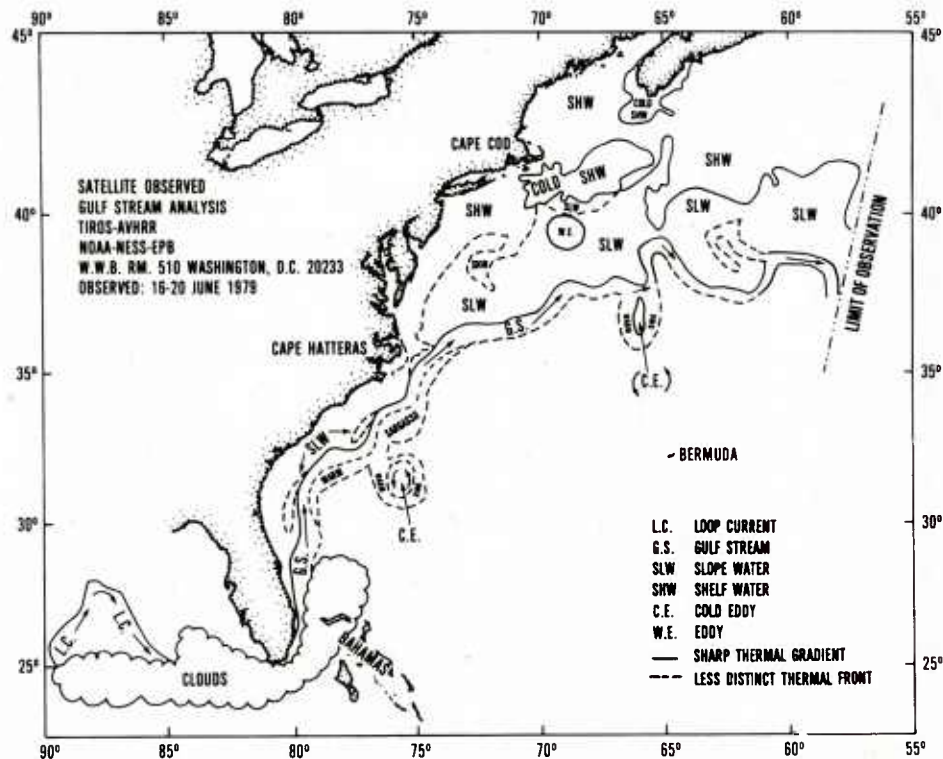


Figure 18. NOAA-NESS Gulf Stream Analysis chart for the period 16-20 June 1979.

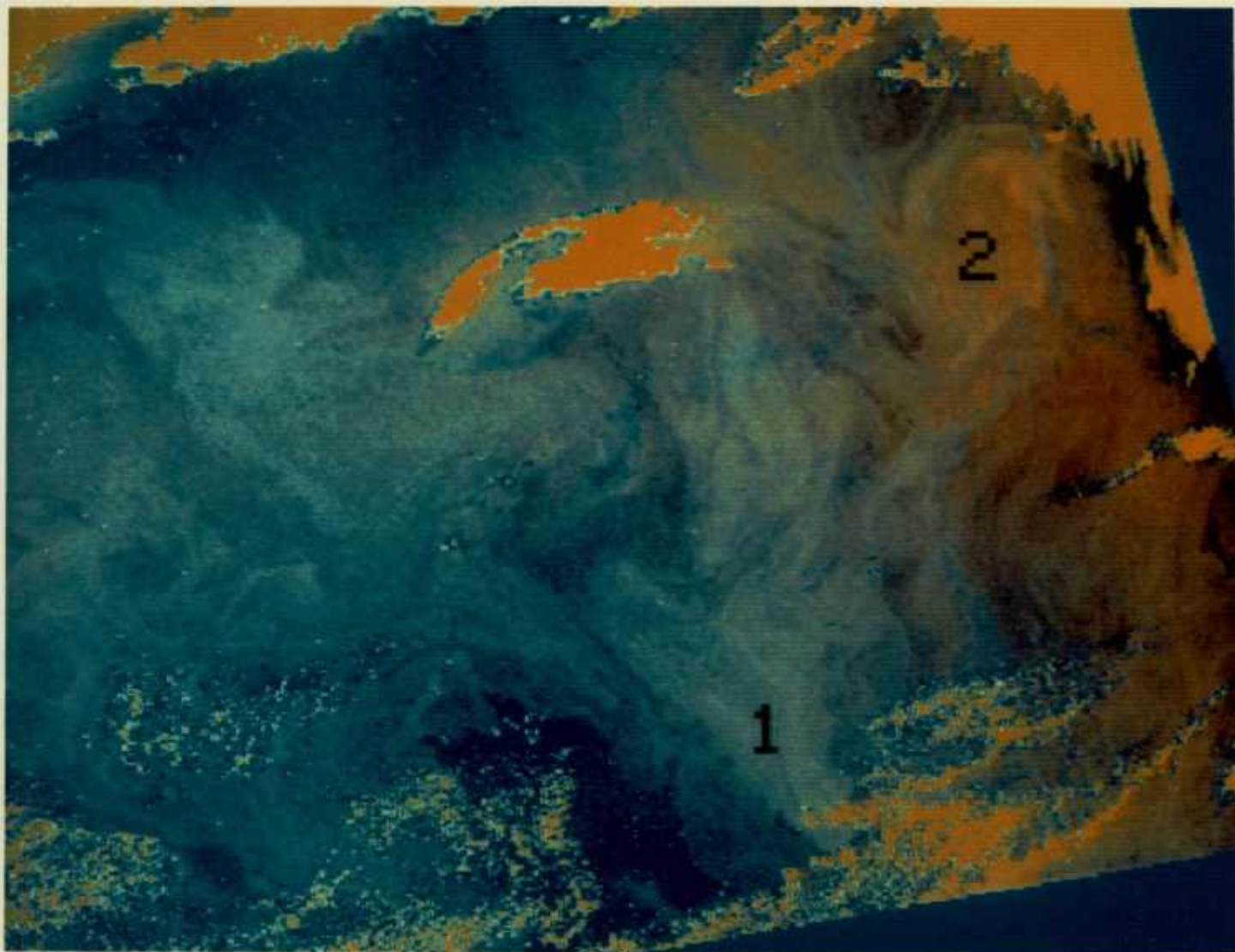


Figure 17. Atmospherically corrected version of Figure 15. Red, green, and blue components of this image come from the second, third, and second minus third principal components respectively.

Table 1 shows there are some notable differences between the data from this example and the Grand Banks CZCS data. In this case, the first (aerosol) principal component contained only 58.1% of the total variance within the PCA box compared to Case I where the aerosol contribution was 96.6% of the total. This variance difference probably results from the combined effects of less atmospheric variability and more upwelled ocean radiance in the Gulf of Mexico data. A similarity between cases I and II is that the third component in both cases seems to contain chlorophyll concentration information. This conclusion, as discussed in Section 3, is based upon the large negative, near zero, and large positive weights for channels 1, 2, and 3, respectively, that go into forming the third component.

Figure 21 shows the first principal component that, under the assumptions of the PCA method, is the atmospheric aerosol contribution to Figure 20. Note that the sun glint band in the center of Figure 20 is present in the first principal component. From this it appears that the PCA atmospheric correction also removes some sun glint. Figure 22 shows this is true. This figure (the third principal component of Figure 20) shows a complete absence of sun glint while still displaying what is believed to be the regional chlorophyll distribution.

4.2.3 Discussion of Case II

The most important oceanic features of Figure 22 are the three distinct eddies, one cold (counterclockwise rotation) and two warm (clockwise rotation). Eddies in



Figure 19. TIROS-N thermal-IR (11.0μ) imagery of the Gulf of Mexico on 19 June 1979 at 0850Z. This is the same image shown as Figure 4, but at a different scale.

the western Gulf of Mexico are observed routinely on IR satellite images during the winter months. However, the image shows to the authors' knowledge, the first summer satellite observation of eddies in the central or western Gulf of Mexico. Note that the TIROS-N IR image for this date (Figure 19) does not show these eddies or the Loop Current inflow through the Yucatan straits (also visible in Figure 22). This is an excellent example of the ability of the CZCS to image mesoscale ocean features through a warm, humid atmosphere where infrared images would not show the features.

A color image formed from the second, third, and fourth principal components of the Case II CZCS image is shown as Figure 23. Note that the Caribbean waters south of the Yucatan straits and the Loop Current inflow are in shades of green, while the coastal and shelf waters of the Gulf of Mexico are in varying shades of blue, purple, and red. One might speculate that the greenish waters within the central Gulf are of Loop Current origin, while the blue/purple/red waters are of Gulf of Mexico origin (river inflow for example). The colors in Figure 23 may, therefore, possibly be used as indicators of water origin, i.e., tracers for general circulation within the Gulf. If this is true, Figure 23 would indicate that most of the water in the west-central Gulf of Mexico is of Loop Current origin. This is consistent with predictive models of the Gulf of Mexico (Hurlburt and Thompson, 1980) that indicate that eddies shed from the Loop Current move toward the west-southwest.

Note that the two eddies in the north central Gulf are positioned along the loop water/shelf water boundary. Interpretation of the color variations indicate that shelf water is entrained along the northern edge of both the warm eddies, and Loop Current water is entrained at the southern edges. These eddies, in effect, appear to be mixing areas for the two contrasting water

types. If this is true, some interesting speculation may be made. Hawkins (1983) has observed very rapid surface cooling of eddies separated from the Loop Current. From considerations of heat content and possible heat fluxes through the sea/air boundary, the observed cooling rates seem to be unrealistically large. Entrainment and subsequent mixing of substantial amounts of shelf water (as the study of Fig. 23 suggests) may explain the rapid decay of eddy surface thermal signatures in this area. Thus, the CZCS may be a tool to disclose mixing processes in the ocean.

4.3 Case III—Gulf of Mexico (Winter)

The Remote Sensing Branch of NORDA conducted a cruise in the Gulf of Mexico in December of 1978. CZCS data from a portion of that cruise period (2 December 1978), has been chosen as a Gulf of Mexico wintertime case study. These data will be compared to XBT, chlorophyll, and other water color related measurements collected during the NORDA cruise.

4.3.1 The Surface Data

The IR imagery used for comparison with the CZCS visible imagery for this case is derived from the CZCS IR channel of the same CZCS data set. Although the CZCS thermal images are crude by comparison with the NOAA imagery, clouds present during the orbits of NOAA-5 and TIROS-N precluded their use, leaving the CZCS orbit the only cloud-free imagery.

The line segment AB in Figure 25 marks an XBT line made from the USNS LYNCH on 6 December 1978, (4 days after the CZCS pass). Figure 24 is a vertical temperature cross section plotted from those XBTs. By convention the Loop Current boundary is considered to be where the 22°C isotherm drops below a depth of 100 m (Leipper, 1970), and from this the line segment AB in Figure 24 straddles the Loop Current boundary. Therefore, the warm (dark) feature seen in the

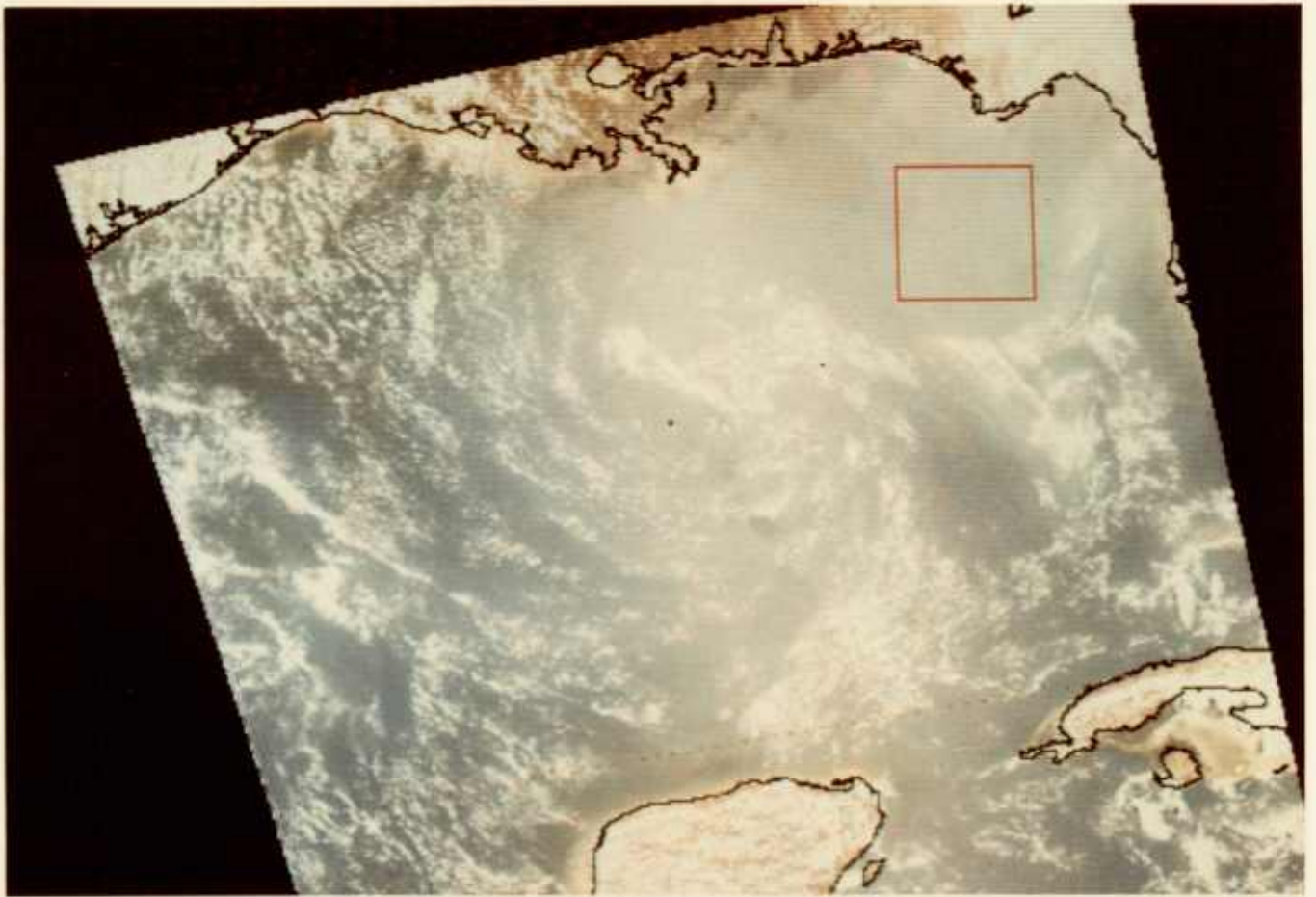
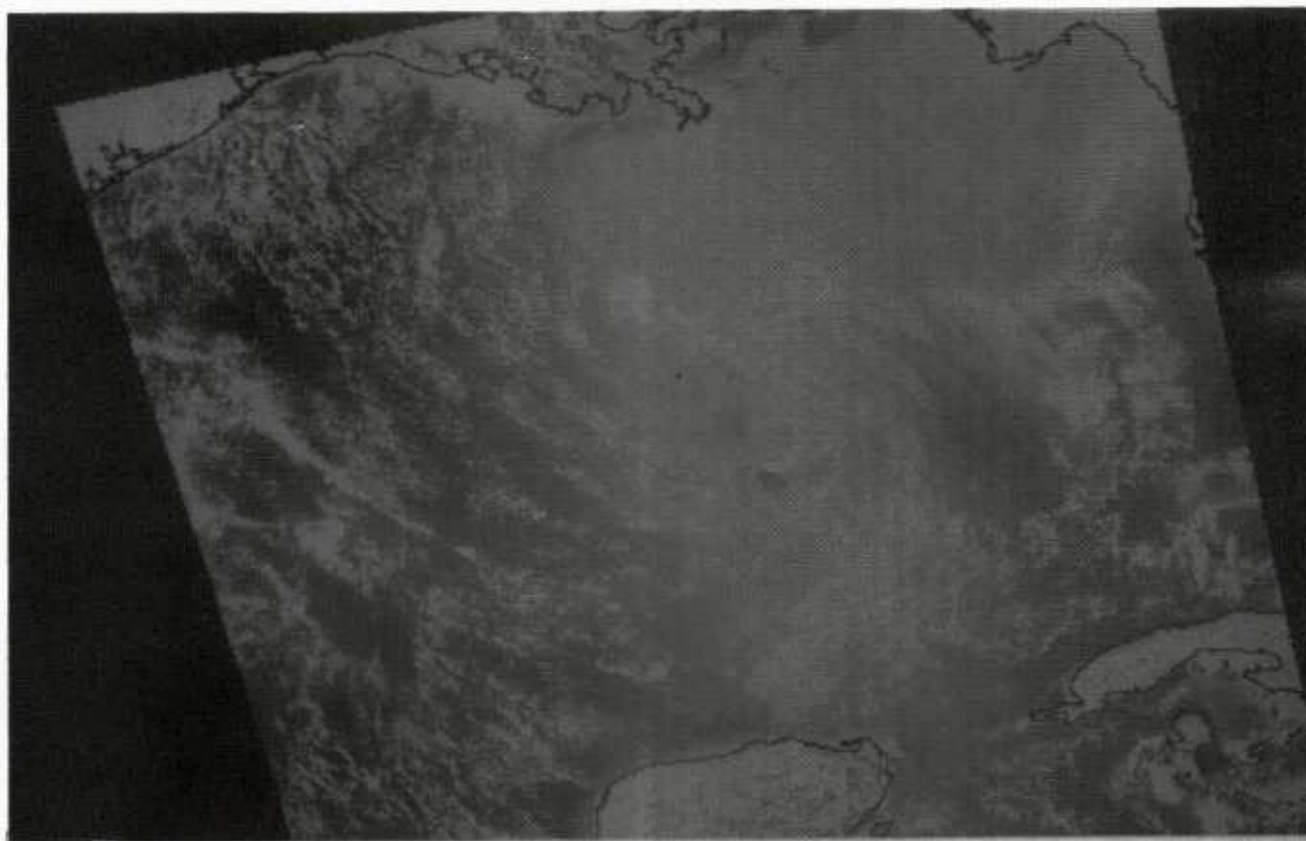


Figure 20. CZCS image formed from bands 1, 2, and 3 of orbit 3310 over the Gulf of Mexico on 19 June at 1729 Z. The red box marks the area included in the PCA analysis.



Figures 21 and 22. First principal component (top) of the Case II CZCS image shown in Figure 20. The third principal component (bottom, primarily showing chlorophyll concentration) of the CZCS image shown in Figure 20.

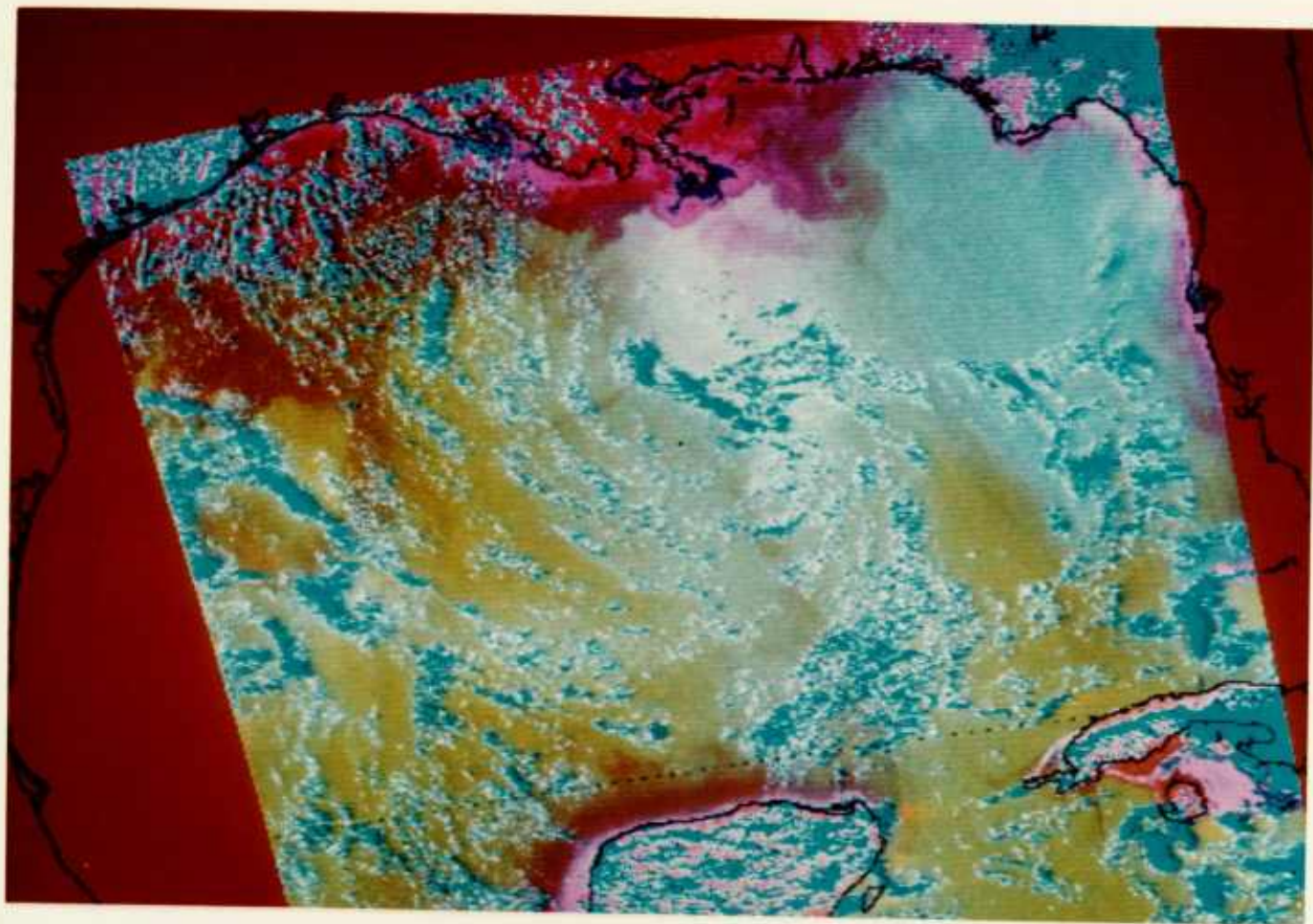


Figure 23. Atmospherically corrected (PCA method) version of Figure 20. CZCS image formed from the second, third, and fourth principal components.

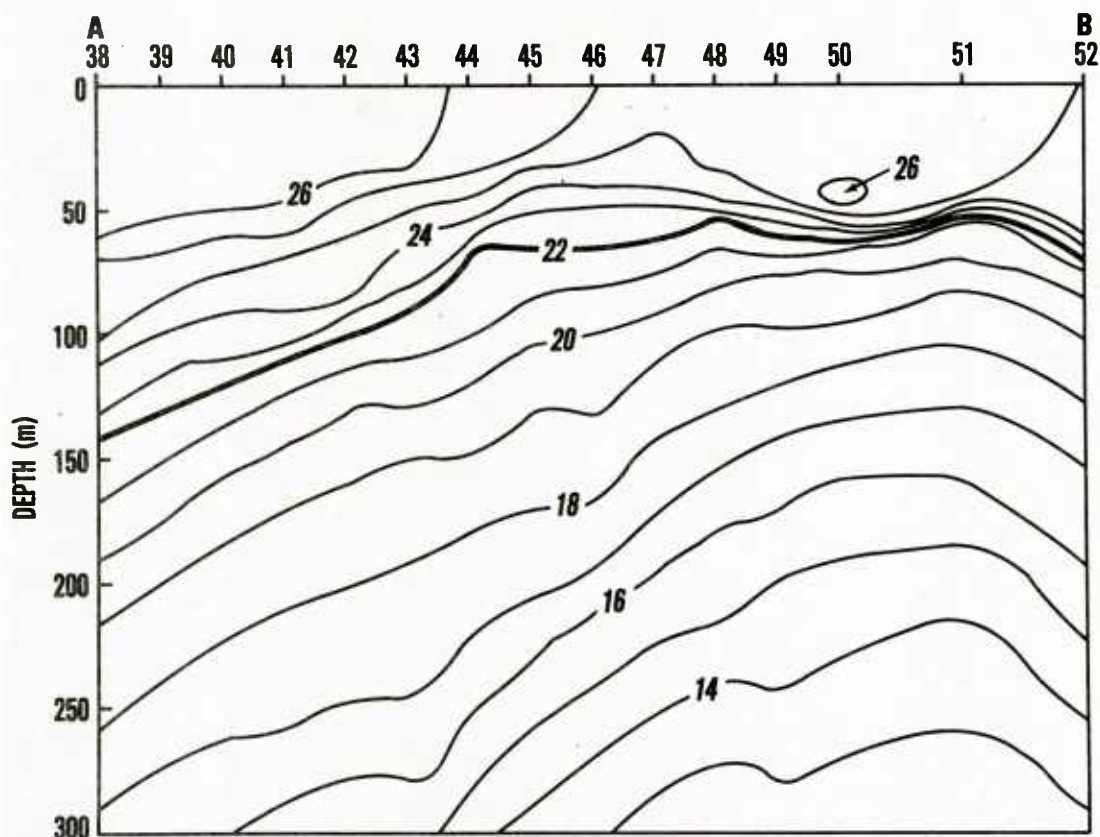


Figure 24. XBT data from along line AB in Figure 25 shown as contours of temperature as a function of position and depth.

south-eastern quadrant of the Gulf is indeed the Loop Current. Furthermore, the XBTs show that the warm feature in the IR imagery is not simply a surface effect, but is associated with oceanic structure that extends at least to the depth range of the XBTs.

Chlorophyll-a concentration and total suspended solids measurements were made on both sides of the Loop Current boundary during the USNS LYNCH cruise. These data show that surface chlorophyll-a concentrations within the Loop Current on 5 December at point A of the line segment AB in Figure 25 was 0.05 mg/l at the surface and 0.30 mg/l at 20 m. Outside the Loop Current at point C in Figure 25, the chlorophyll-a concentration at depths of 2 and 20 m was 0.19 and 0.14 mg/l when measured on 12 December.

Although these two measurements were 7 days apart and neither coincided with the CZCS data on 2 December, these data show that a large difference in the vertical distribution of chlorophyll-a did exist between Loop Current and Gulf waters. Although the values on 2 December may have been different, these measurements indicate that a strong chlorophyll-a change did take place across the Loop Current boundary. Total suspended solids at these stations (average of surface and 20-m depth values) were 490 ug/l at point A and 195 ug/l at point C indicating that solids other than chlorophyll-a were also in the water in varying concentrations. These measurements would suggest that one could expect to see a color difference between the resident Gulf of Mexico and Loop Current waters.

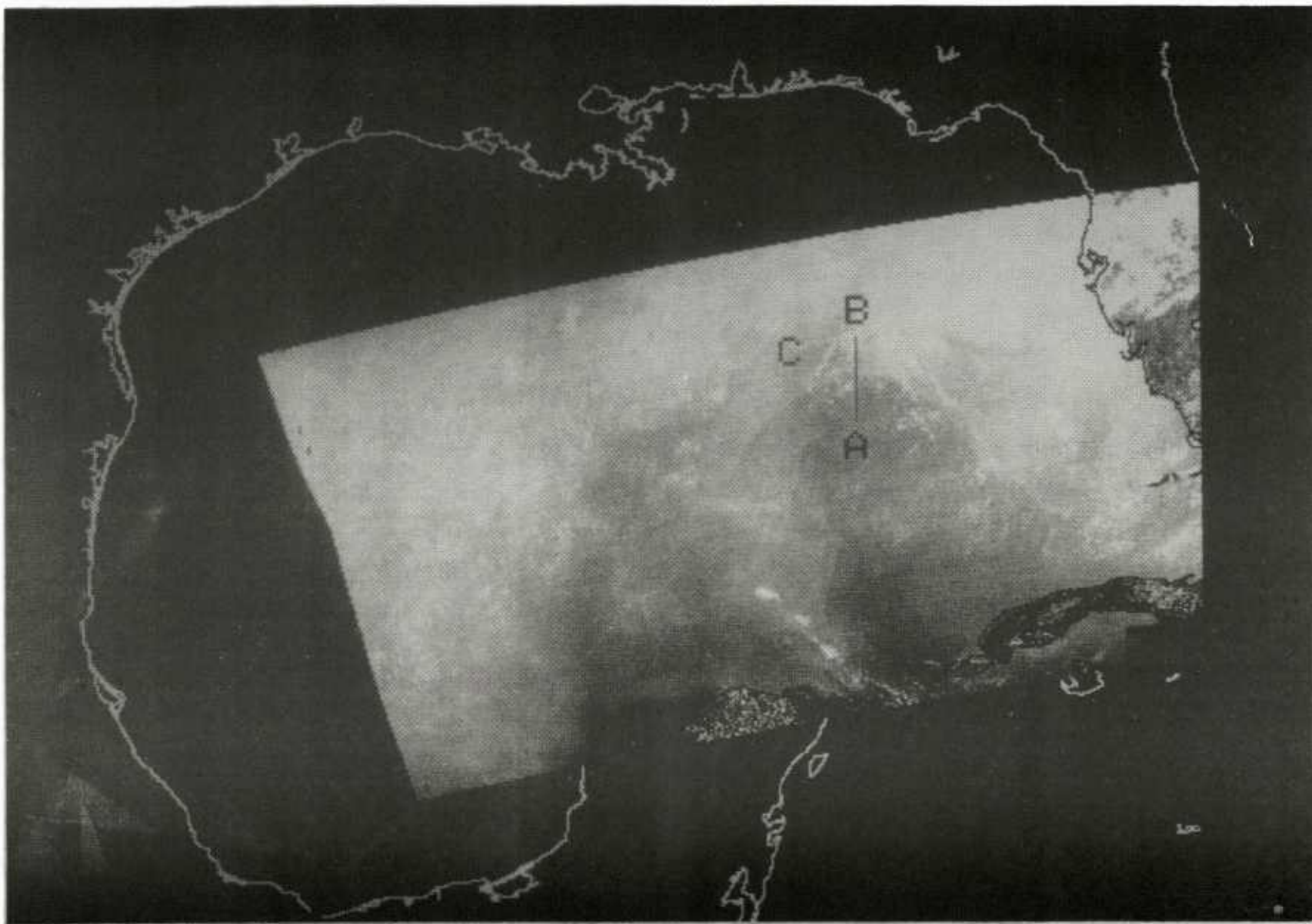


Figure 25. CZCS channel 6 (thermal IR) from orbit 545 over the Gulf of Mexico on 2 December 1978 at 1715Z. The line AB marks the location of an XBT transect by the USNS LYNCH on 6 December 1978.

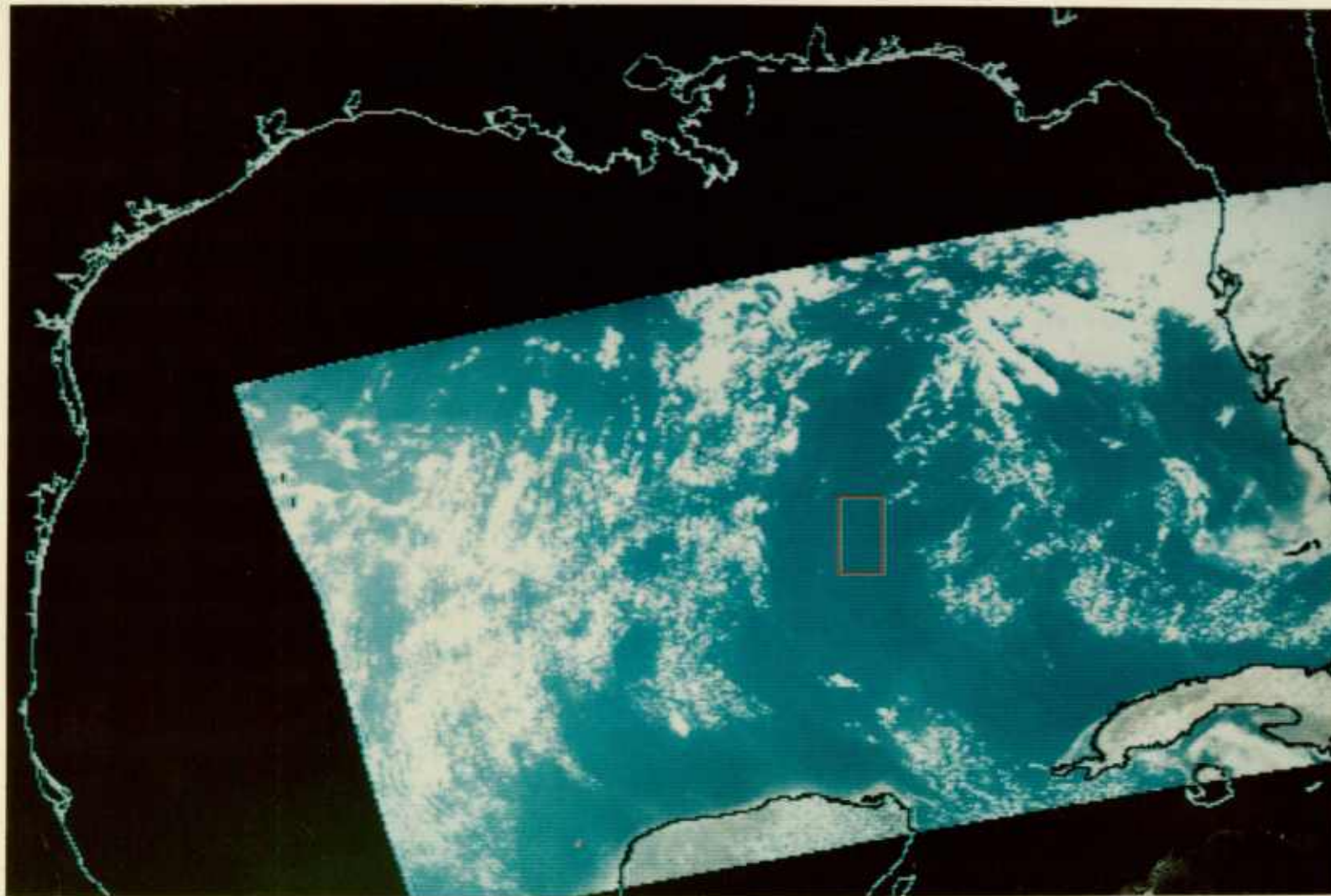


Figure 26. CZCS image formed from bands 1, 2, and 3 of orbit 545 over the Gulf of Mexico on 2 December 1978 at 1715 Z. The red box marks the area included in the PCA analysis.

4.3.2 The CZCS Data

Figure 26 is a color image formed from channels 1, 2, and 3 of CZCS orbit 545 on 2 December 1978. This image has been transformed to Mercator projection with the same 3.3 km/pixel scale as Case II. The image subarea chosen for PCA analysis is indicated by the red box in the figure. Data statistics within the box are as follows:

Case III Gulf of Mexico PCA Box Statistics

mean = 168.6, 133.6, 131.0, 116.7
std dev = 1.52, 1.73, 2.31, 4.47
eigenvalues = 0.893, 0.069, 0.023, 0.014

	0.180	0.293	0.410	0.844
a_{kj}	-0.723	-0.371	-0.358	0.458
	-0.616	0.167	0.718	-0.275
	0.252	-0.864	0.432	0.036

As in the previous cases the a_{kj} matrix shows a component (the third one in this case) that seems to capture chlorophyll-a variability with its -0.616, -0.167, and 0.718 weights in channels 1, 2, and 3 respectively. Figure 27 shows the first principal component that, under the assumptions of the PCA method, is the atmospheric aerosol contribution to Figure 26.

4.3.3 Discussion of Case III

An atmospherically corrected Case III CZCS color image (Fig. 28) formed from principal components 2, 3, and 4 shows the Loop Current boundary to be in the same location as that shown by XBT data in Figure 24. The position and shape of the Loop Current pattern in the color image corresponds with the position and shape of the warm feature in the thermal image (Fig. 24) indicating that the color scanner is indeed imaging the Loop Current. The Loop Current is the only major deep-ocean feature apparent in Figure 28. This is consistent with the finding of the USNS LYNCH data that

showed that no eddies or major oceanographic features, other than the Loop Current, were found in the eastern Gulf at the time.

The main conclusion to be drawn from Case III is that the Loop Current appears to have a color signature in the wintertime as well as in the Case II summertime image. This would tend to indicate a persistence in the color uniqueness of the Loop Current throughout the year. This is important from a Navy point of view since if the Loop Current, or other similar mesoscale features, possessed an observable color signature only during short-lived transient biological events, the utility of ocean color for Navy operations would be diminished.

4.4 Case IV: Mediterranean

NORDA scientists participated in an international oceanographic experiment, called ¿Donde Va?, conducted in the western Mediterranean in October 1982 (La Violette, et al. 1982; Kinder, 1983). The study focused on the Alboran Gyre, a large eddy found in the western Alboran Sea. The Alboran Sea is an oceanographically dynamic area where Mediterranean, Atlantic, locally upwelled, and coastal waters constantly interact. This area, therefore, tends to produce a wide variety of ocean color signatures that can be easily sensed by the CZCS.

4.4.1 The Surface Data

During the period 6-18 October 1982, ship, aircraft, and satellite data were collected as part of the ¿Donde Va? experiment in the Alboran Sea (La Violette, 1983). The ship data included CTD, XBT, and chlorophyll measurements, whereas the aircraft data included sea surface temperature, sonobuoy drift, and wind measurements. The satellite data, acquired every 12 hours, included infrared and visible measurements that were registered and atmospherically corrected

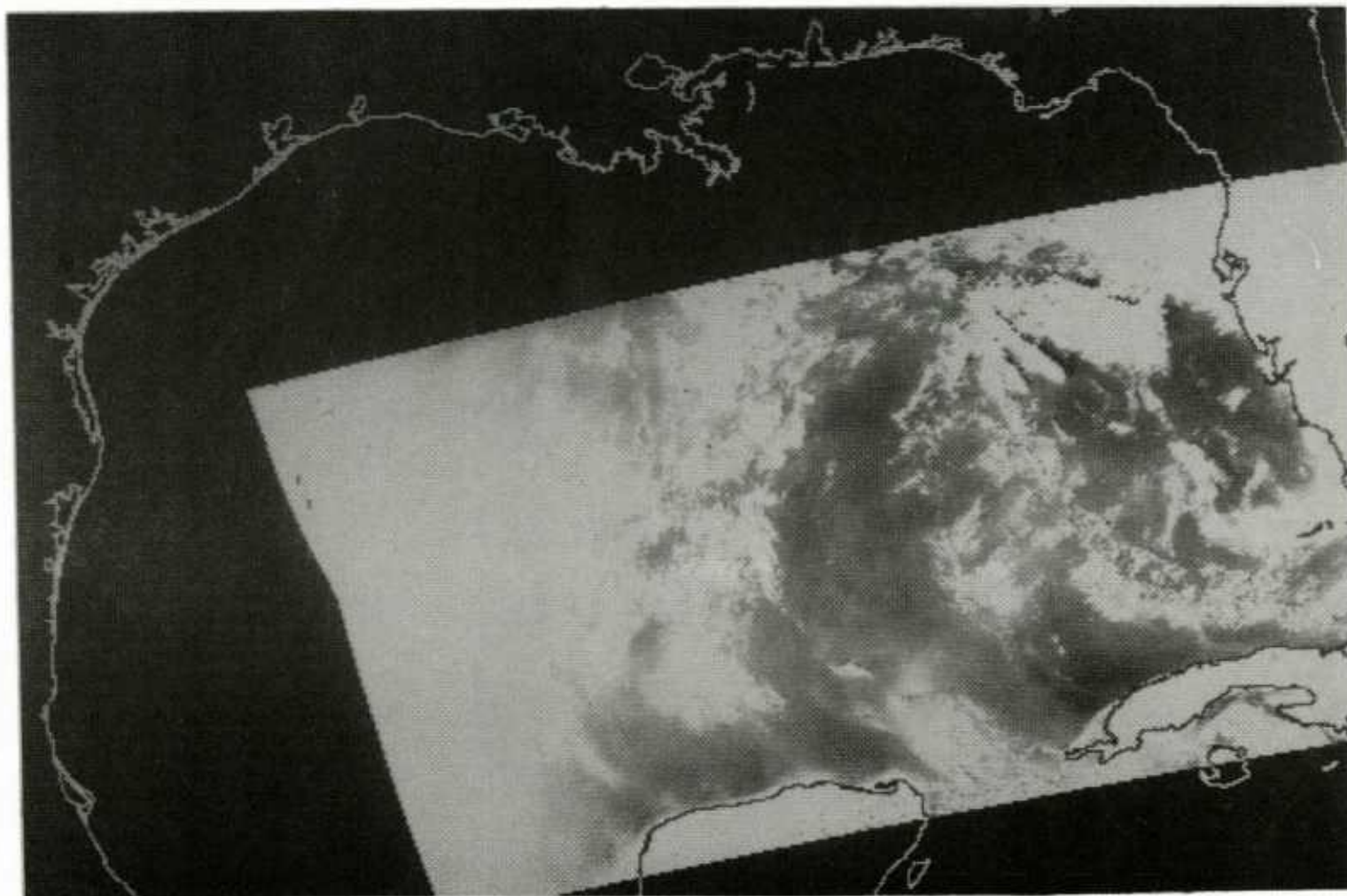


Figure 27. The first principal component (aerosol) of the Case III CZCS image.

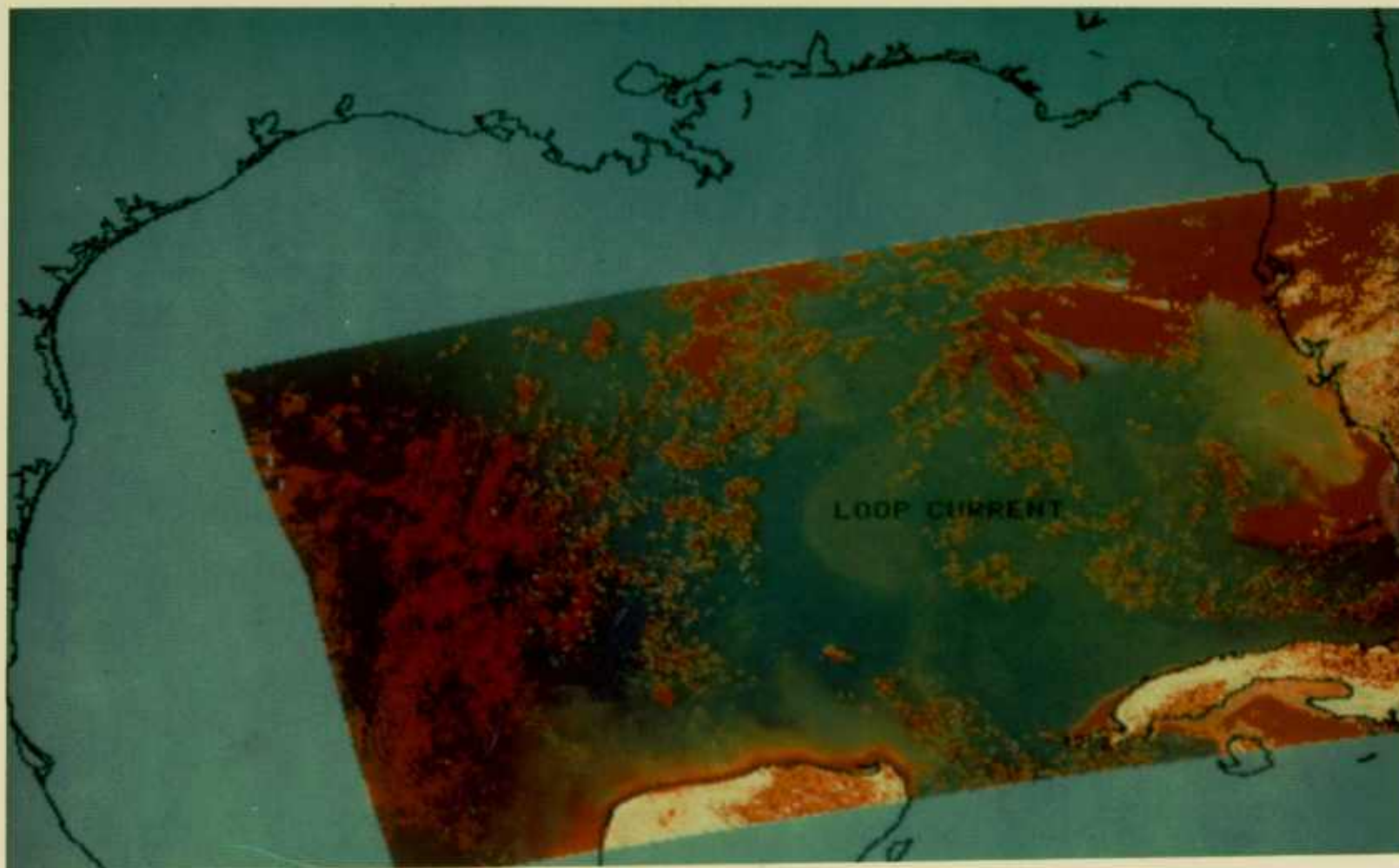
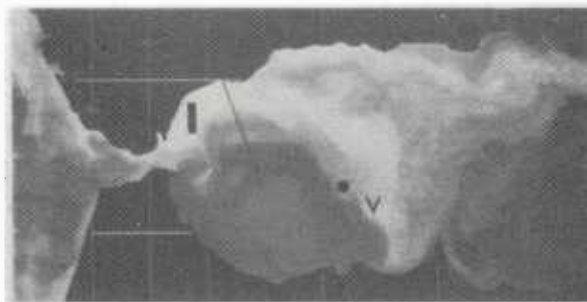
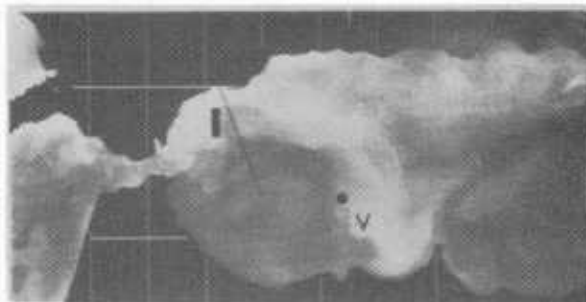


Figure 28. Color image formed from the second, third, and fourth principal components of the Case III CZCS image.

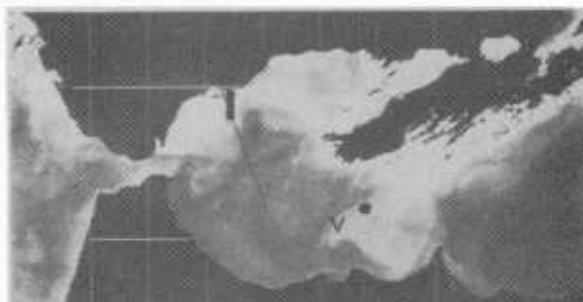
0349 GMT 11 OCTOBER 1982



1513 GMT 11 OCTOBER 1982



0337 GMT 12 OCTOBER 1982



1501 GMT 12 OCTOBER 1982



1449 GMT 13 OCTOBER 1982

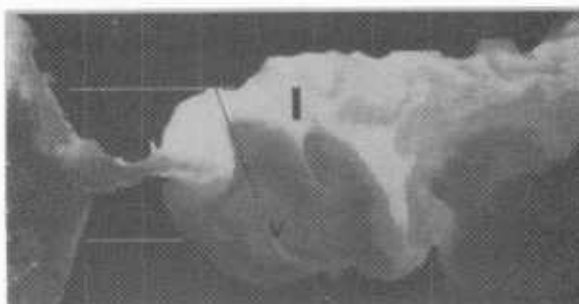


Figure 29. NOAA-7 infrared imagery for the early morning of 11 October through the afternoon of 13 October 1982.

to form sea surface radiation images for the study period. Analysis of these measurements shows that incoming Atlantic water, as it left the Strait of Gibraltar, moved at the surface in a narrow (approximately 16 km wide) band of approximately 17-18°C water that formed the initial quarter of the circumference of the gyre. As the water continued the incoming water was modified; however, it still retained its identity. Associated with the inflowing band of water were cold water features that hung southward toward the center of the gyre. These also moved around the gyre, changing shape as they moved.

The five-image sequence of Figure 29 shows the movement of several of these mesoscale cold-water features around the gyre. Notice the feature developing on 12 October in the region east of Gibraltar. An enlargement of the IR image for the afternoon of 12 October (1501 hrs GMT) is presented in Figure 30 together with the principal component for chlorophyll from the Nimbus-7 CZCS visible image of the same area for 1155 hrs GMT of the same day. Ship data taken for the same period show the pattern of distribution of the chlorophyll to be similar to that shown by the satellite imagery. Examination of the NOAA imagery shows that the predominant feature moved approximately 17 km in the 11 hours from the time of the morning NOAA IR image to the time of the afternoon NOAA IR image, or at an average speed of approximately 0.4 m/sec. The CZCS image indicates a movement of approximately 9 km in the time between the Nimbus-7 noon pass and the NOAA afternoon pass (i.e., if one assumes that the sharpest gradient change in the CZCS image is directly associated with the sharpest thermal gradient in the NOAA imagery). This equates to a movement of 0.8 m/sec or twice the rate of movement for the 11-hour period between the two NOAA images. The figure gives a graphic indication of how much movement can take place in 4 hours. The possible reason for the variations in speed is the phase of the

diurnal tide. Comparison of the shifts in speed with the tide tables from Ceuta show the two are in phase.

4.4.2 The CZCS Data

Eleven essentially cloud-free CZCS images were collected for the ¿Donde Va? investigations during the first 3 weeks of October 1982. The 12 October image chosen for analysis here is the poorest image of the ¿Donde Va? data set in terms of atmospheric contamination. Many of the images during the experiment were useable for descriptive analysis without any atmospheric correction, but the 12 October image (Fig. 31) is so severely contaminated by atmospheric aerosols that ocean color features are completely masked. This image is used as the fourth case study in order to evaluate the PCA atmospheric correction method on an extreme case.

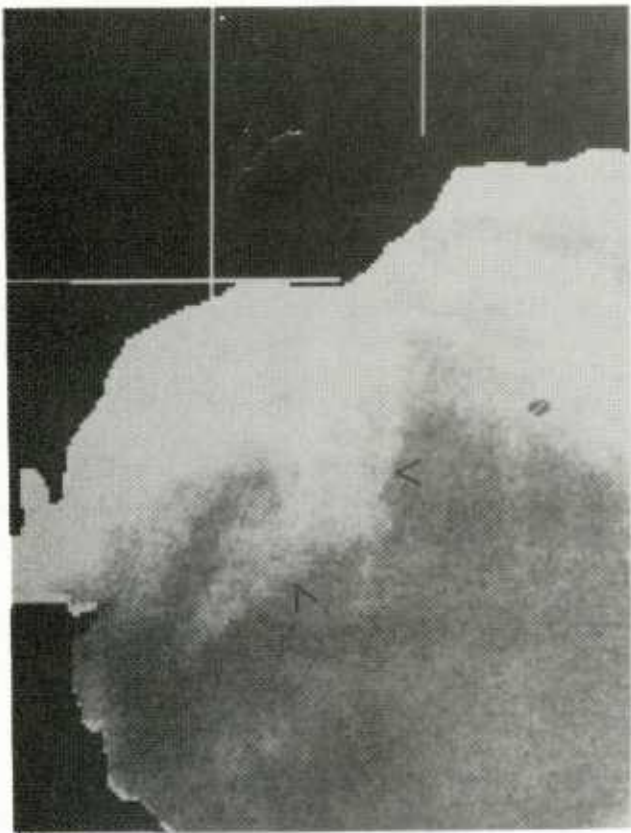
The PCA analysis was performed on the area shown by the red box in Figure 31. Statistics for the PCA box are as follows:

Case IV Mediterranean PCA Box Statistics

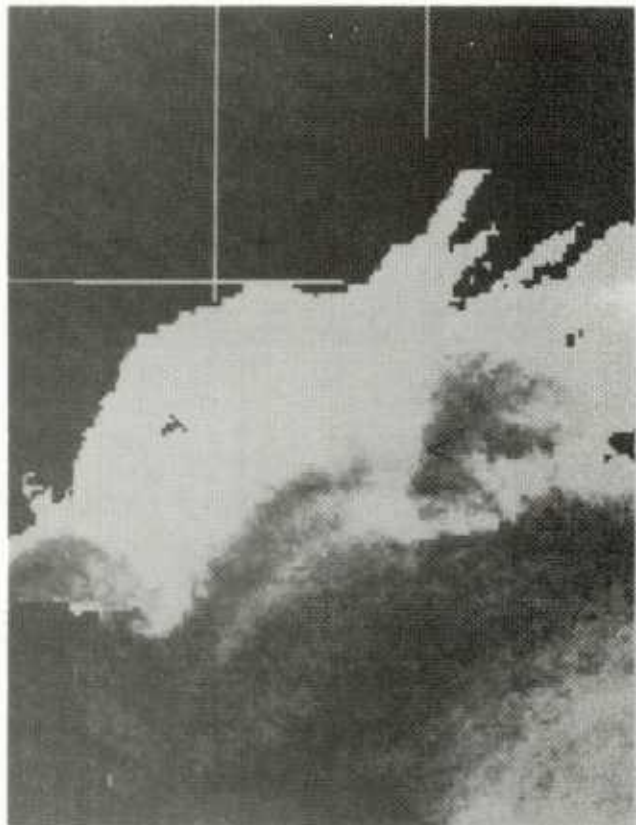
mean = 107.8, 111.1, 117.9, 129.4
std dev = 3.47, 6.13, 8.15, 15.62
eigenvalues = .986, .008, .004, .001

	0.172	0.319	0.428	0.827
a_{kj}	-0.173	-0.552	-0.594	0.557
	0.969	-0.137	-0.198	-0.046
	0.023	-0.756	0.651	-0.049

Figure 32 is the first principal component (atmospheric aerosol) of the Case IV CZCS image. Figure 33 is a false color image produced by principal components 2, 3, and 4 that contribute red, green, and blue to the color image. Figure 33 represents the atmospherically-corrected Case IV CZCS image. The anti-cyclonic circulation of the Alboran gyre is seen in Figure 33 in shades of gold. Patterns created by turbid coastal waters are seen in shades of purple along the African coast.



NIMBUS 7 CZCS



NOAA 7 AVHRR-IR

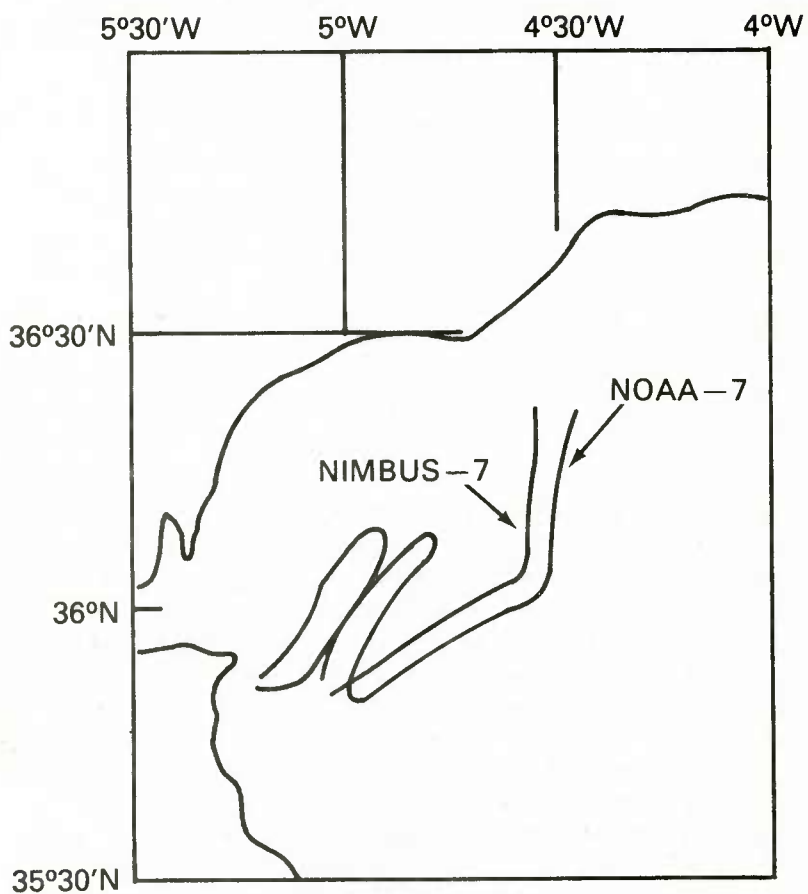


Figure 30. The short term movement of feature shown by Nimbus CZCS and NOAA-7 AVHRR-IR imagery. The movement took place between 1155 (Nimbus) and 1501 (NOAA) hrs GMT on 12 October.



Figure 31. CZCS image formed from bands 1, 2, and 3 of orbit 20029 over the Mediterranean Sea on 12 October 1982 at 1126 Z. The yellow box marks the area included in the PCA analysis.

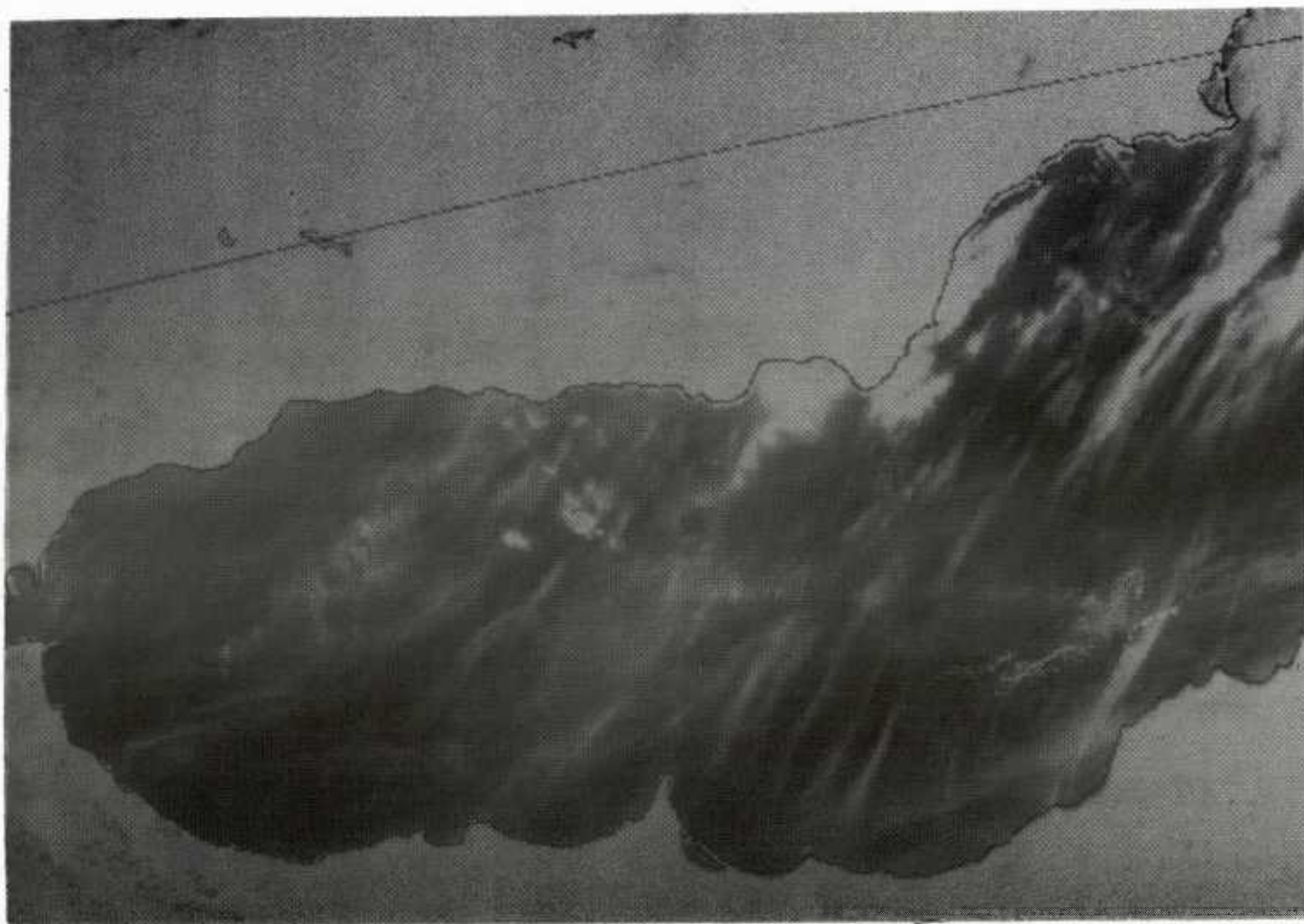


Figure 32. First principal component of the Case IV CZCS image shown in Figure 30. Under the PCA method of atmospheric correction, this is taken to be the aerosol contribution to the image.

4.4.3 Discussion of Case IV

The PCA method seems to have done a reasonable job of extracting water color features through this very hazy atmosphere. Comparison of Figure 33 with the NOAA-7 IR image for the same day (Fig. 34) shows that most of the ocean features apparent in the IR image are also seen in the atmospherically corrected CZCS image. However, some uncorrected artifacts of the atmosphere do remain in Figure 33.

The difference in color shades for the Alboran gyre and the coastal features in Figure 33 is of interest in this case. It appears that the PCA transformation has separated the chlorophyll (Alboran gyre) and inorganic sediment (coastal features) contributions to the water color into different principal components. Looking at the individual principal components that make up the image in Figure 33, we find that coastal patterns appear in the second component (Fig. 35), which does not show the gyre at all. The gyre appears in the third component (Fig. 36) that exhibits only a very faint trace of the coastal features. The authors have processed a Gulf of Mexico data set (not included as a case study here) where a similar separation of chlorophyll and sediment seems to have occurred.

5. Universal Quick-Look CZCS Atmospheric Correction Algorithms

In each of the case studies, we employed Principal Components Analysis to derive a transformation matrix that when applied to the original CZCS spectral bands produced a new multibanded image with the atmospheric radiance largely confined to a single band; the other bands are predominantly composed of ocean radiance. The result of using this transformation matrix, therefore, is a form of atmospheric correction. The question is now asked, "How similar are these transformation matrices from case

to case?" If there is a strong similarity, then a universal set of matrix coefficients could be defined that could be used for atmospheric correction on most images without requiring the PCA procedural step.

In the discussion of the previous sections, some similarity has been noticeable. All cases resulted in a chlorophyll-like principal component where large negative, near zero, and large positive coefficients for channels 1, 2, and 3, respectively, seemed to reflect the chlorophyll "hinge point" behavior. The most striking similarity observed is between case studies I and III, Grand Banks and Gulf of Mexico winter, where the "chlorophyll component" weights, shown in the table below, are very similar.

Chlorophyll Component Coefficients

	CH1	CH2	CH3	CH4
Case I	-0.529	0.199	0.743	-0.356
Case III	-0.616	0.167	0.718	-0.275

The PCA boxes for these two cases were offshore, well away from any influence of coastal or shelf-type waters. This type of location may explain their similarity. If so, then an average of these two sets of weights might be a good first approximation to a universal atmospheric correction algorithm that would result in delineation of chlorophyll patterns for deep ocean waters. Such an algorithm would be

$$\text{deep ocean chlorophyll} = -0.572 \cdot \text{Ch1} + 0.183 \cdot \text{Ch2} + 0.730 \cdot \text{Ch3} - 0.315 \cdot \text{Ch4} \quad (7)$$

where Ch1, Ch2, Ch3, and Ch4 are the raw digital counts in each of the first 4 CZCS spectral channels.

For case studies II and IV, Gulf of Mexico summer and Mediterranean, the boxes selected for PCA were in shelf waters. These two cases both resulted in "chlorophyll components" that were also

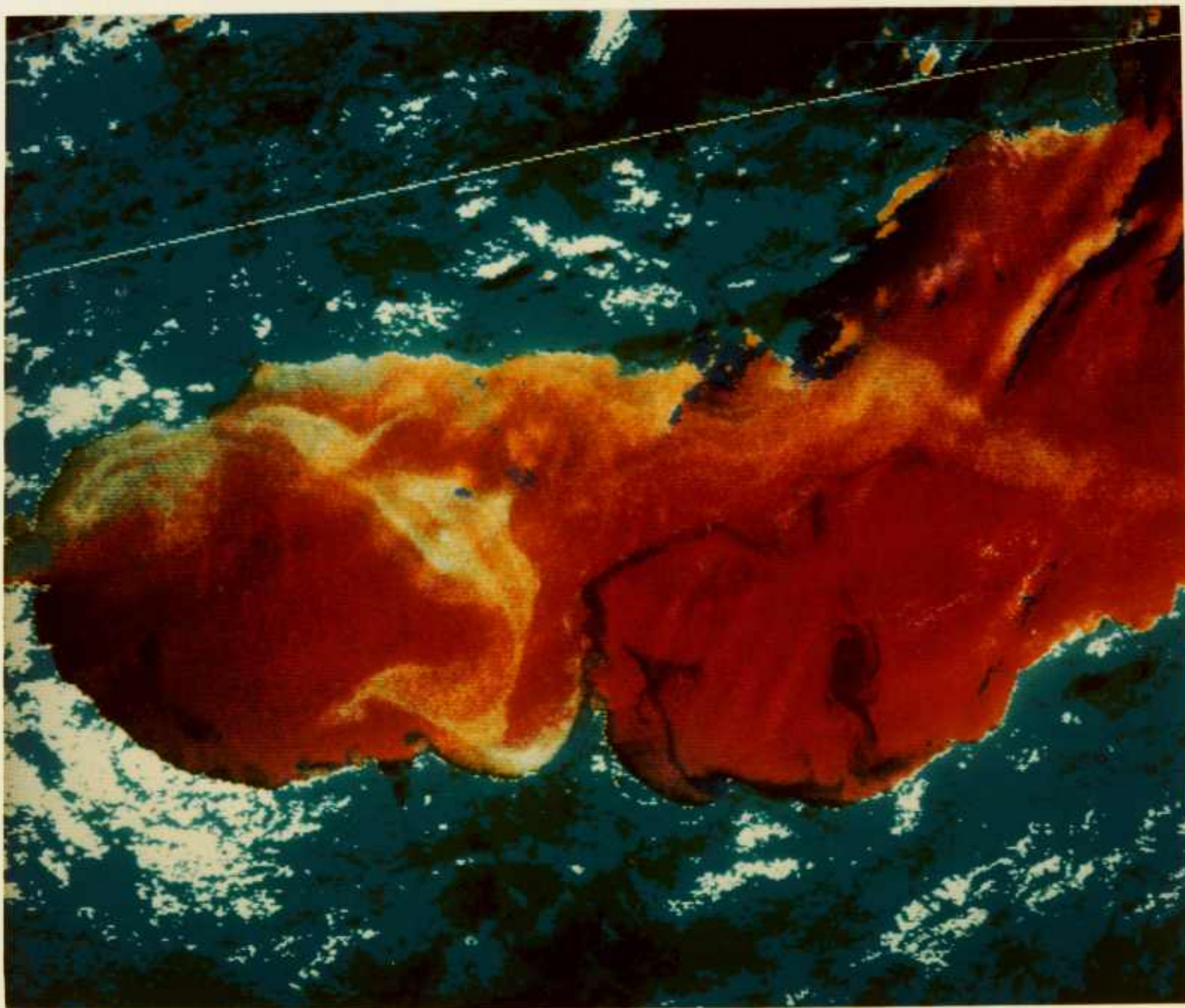


Figure 33. Atmospherically corrected (PCA method) version of Figure 31 CZCS image formed from the second, third, and fourth principal components.

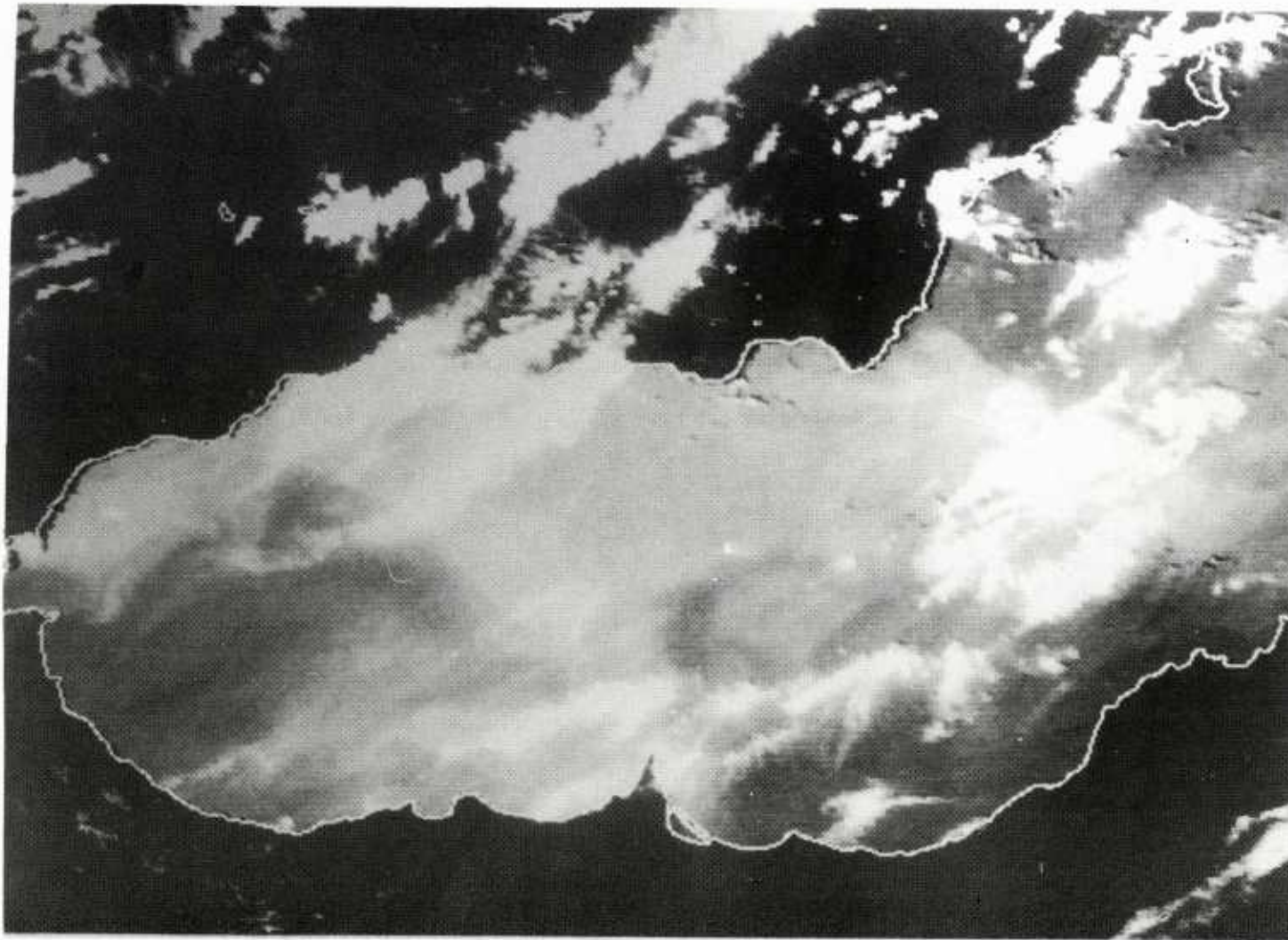


Figure 34. NOAA-7 thermal IR ($11.0\ \mu$) imagery of the Alboran Sea on 12 October 1982 at 1505Z.

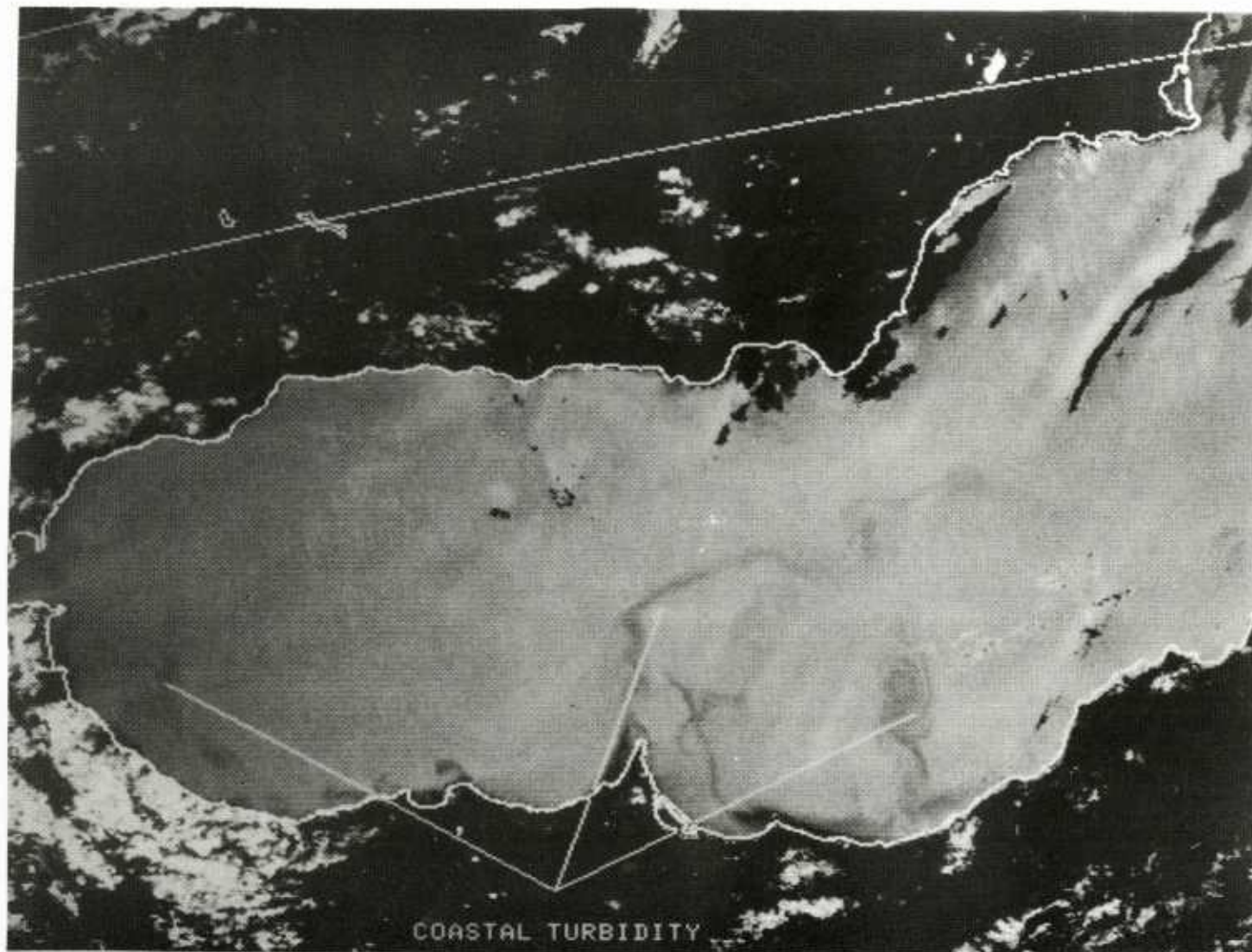


Figure 35. The second principal component for the Case IV CZCS image. Image shows primarily the coastal features along the African coast. Evidence of the Alboran gyre is absent.

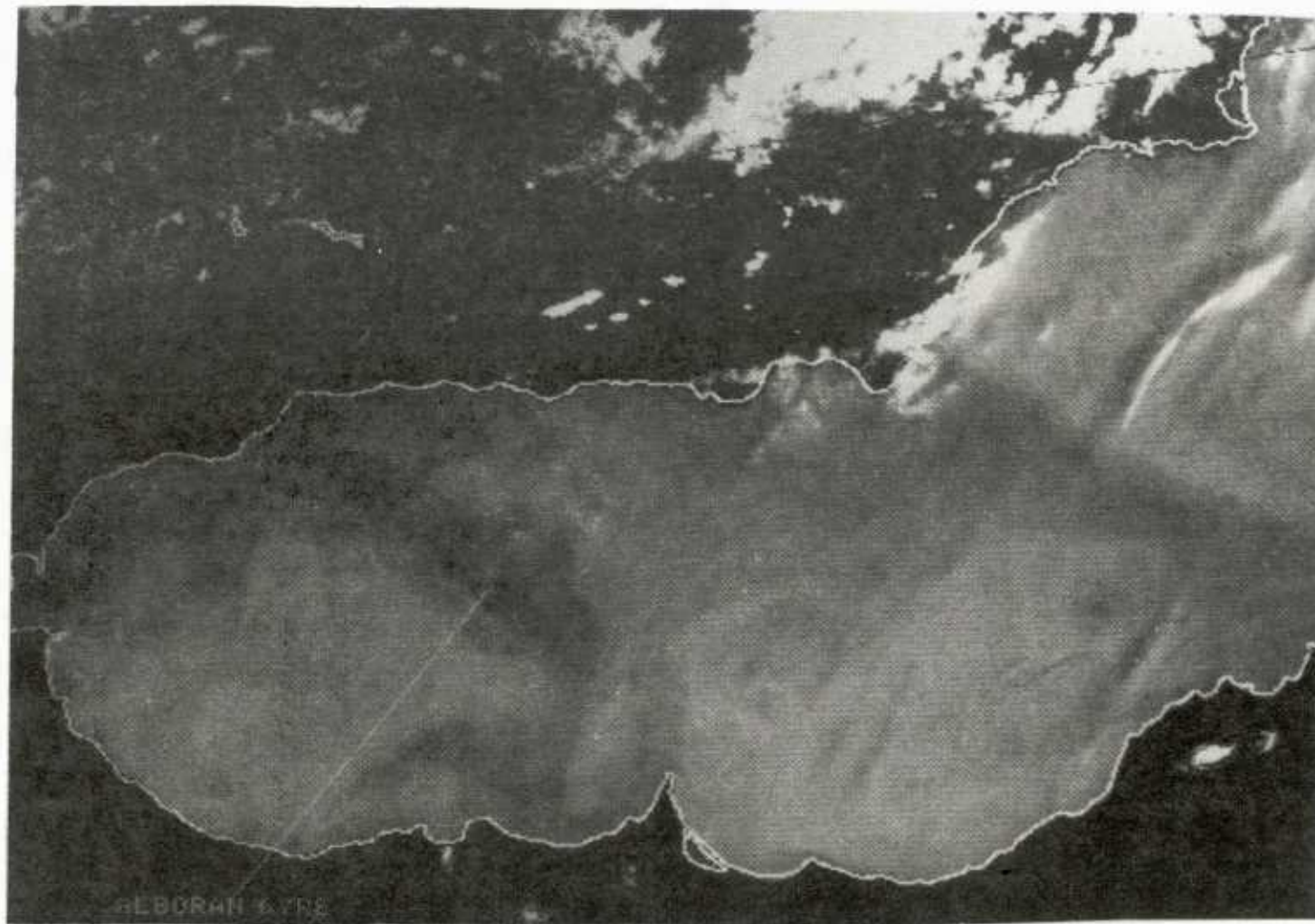


Figure 36. The third principal component for the Case IV CZCS image. Image clearly shows the position of the Alboran gyre.

similar to each other, but significantly different from the Case I and III results from PCA in open ocean waters. The table below gives the "chlorophyll component" weights for cases II and IV.

Chlorophyll Component Coefficients

	Ch1	Ch2	Ch3	Ch4
Case II	-0.849	0.284	0.405	-0.181
Case IV	-0.969	0.137	0.198	0.046

These two sets of numbers are similar, but not as closely matched as the Case I and III deep water values. More variability in shelf areas is probably to be expected because of the greater variability of water types.

Here again, we propose that the average of these two sets of coefficients might be a first guess for a usable, universal, quick-look algorithm for imaging chlorophyll distribution in shelf waters. The algorithm would be

$$\text{shelf chlorophyll} = -0.909 \cdot \text{Ch1} + 0.210 \cdot \text{Ch2} + 0.301 \cdot \text{Ch3} - 0.067 \cdot \text{Ch4} \quad (8)$$

How well would one expect a universal algorithm to perform on a CZCS image that is not one of the case studies presented here? The spectral variability of aerosol phase functions, CZCS radiometric calibration uncertainties, and many of the same factors that make the single-scattering method difficult to use also introduce variability that would tend to degrade the performance of any universal algorithms. However, it is believed that the degradation resulting from these factors will not be sufficiently large to prevent their use for many Navy operational or descriptive applications.

To illustrate this point, the universal algorithm's coefficients proposed here have been applied to a fifth CZCS image of the Gulf of Tehuantepec off the west coast of Mexico. The original CZCS image recorded on 30 November 1981 is shown in

Figure 37. The results of the deep ocean and shelf water chlorophyll algorithms are shown as Figures 38 and 39, respectively. These figures do show a significant reduction in atmospheric haze, thus permitting improved display of the ocean mesoscale color patterns.

6. Summary and Conclusions

Previous methods that perform atmospheric corrections on CZCS data based on single-scattering theory are shown in this report to be difficult to use. This arises from uncertainties concerning the spectral dependency of the aerosol phase function, instrument calibration, as well as the validity of the single-scattering approximation for optically thick atmospheres. A statistical approach based on Principal Components Analysis that avoids many of these problems is presented.

The statistical method, unlike the methods based on single-scattering theory, does not result in quantitative estimates of spectral radiance. The PCA correction method is, therefore, not proposed as a replacement for the single-scattering methods in those applications where spectral radiance measurements are needed. The new method is useful for those cases where a descriptive interpretation of the corrected imagery is required.

The four case studies analyzed seem to indicate that mesoscale features in the deep ocean are frequently discernable in atmospherically corrected CZCS imagery. The case study of the Alboran Sea showed the features could be used as part of the analysis of the movement of mesoscale features. Thus, the use of this type of data is promising for Naval applications where mesoscale structure must be identified and monitored. The corrected imagery has been shown to have other uses in these case studies. The summertime Gulf of Mexico case study has demonstrated the imaging of mesoscale

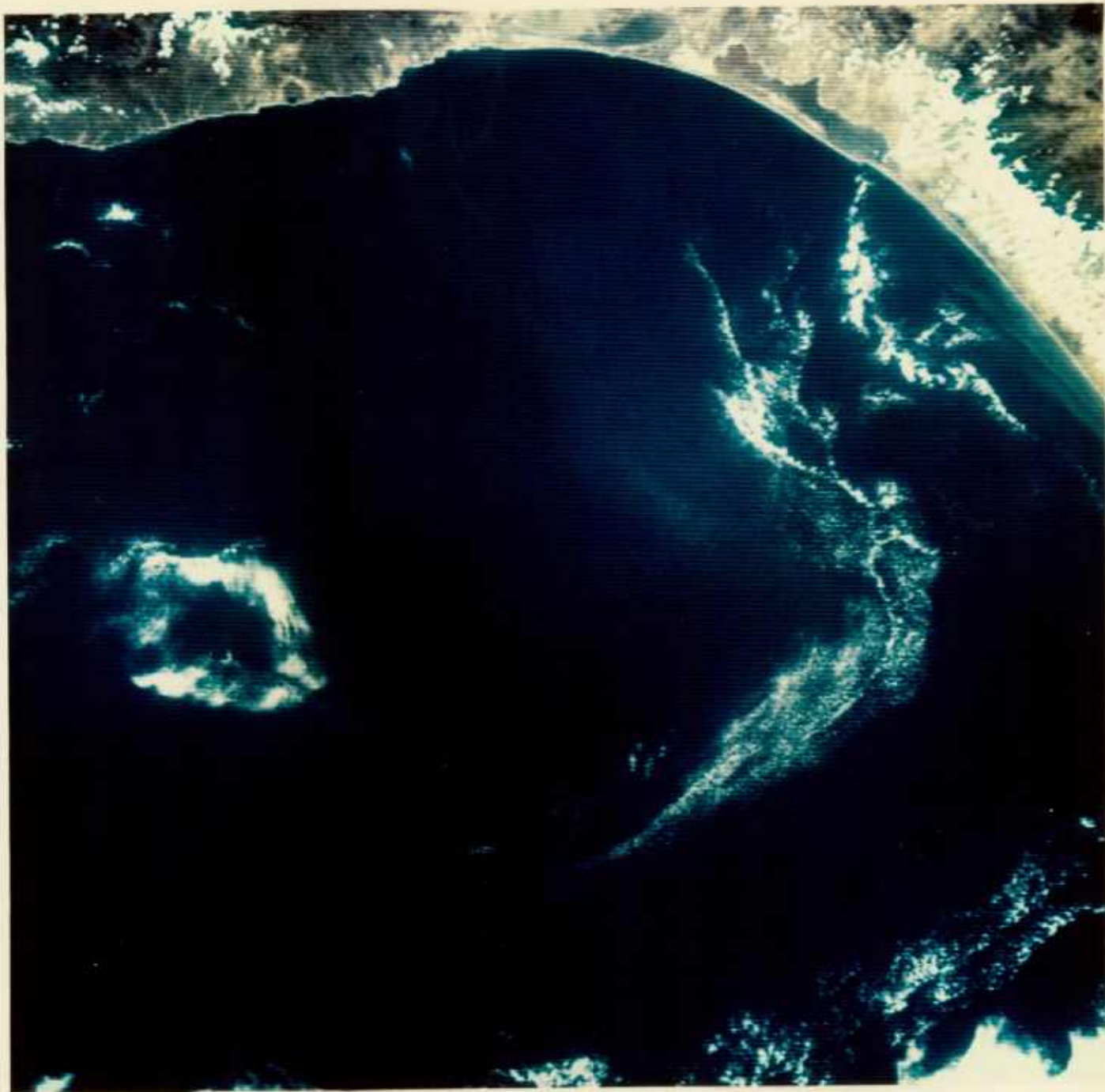


Figure 37. Color image formed from CZCS bands 1, 2, and 3 on orbit 15665 at 1750 Z on 30 November 1981. Area shown is the Gulf of Tehuantepec on the Pacific Coast of Mexico.



Figure 38. Image formed from application of the universal deep-water algorithm (Eq. 7) to the image of Figure 37.

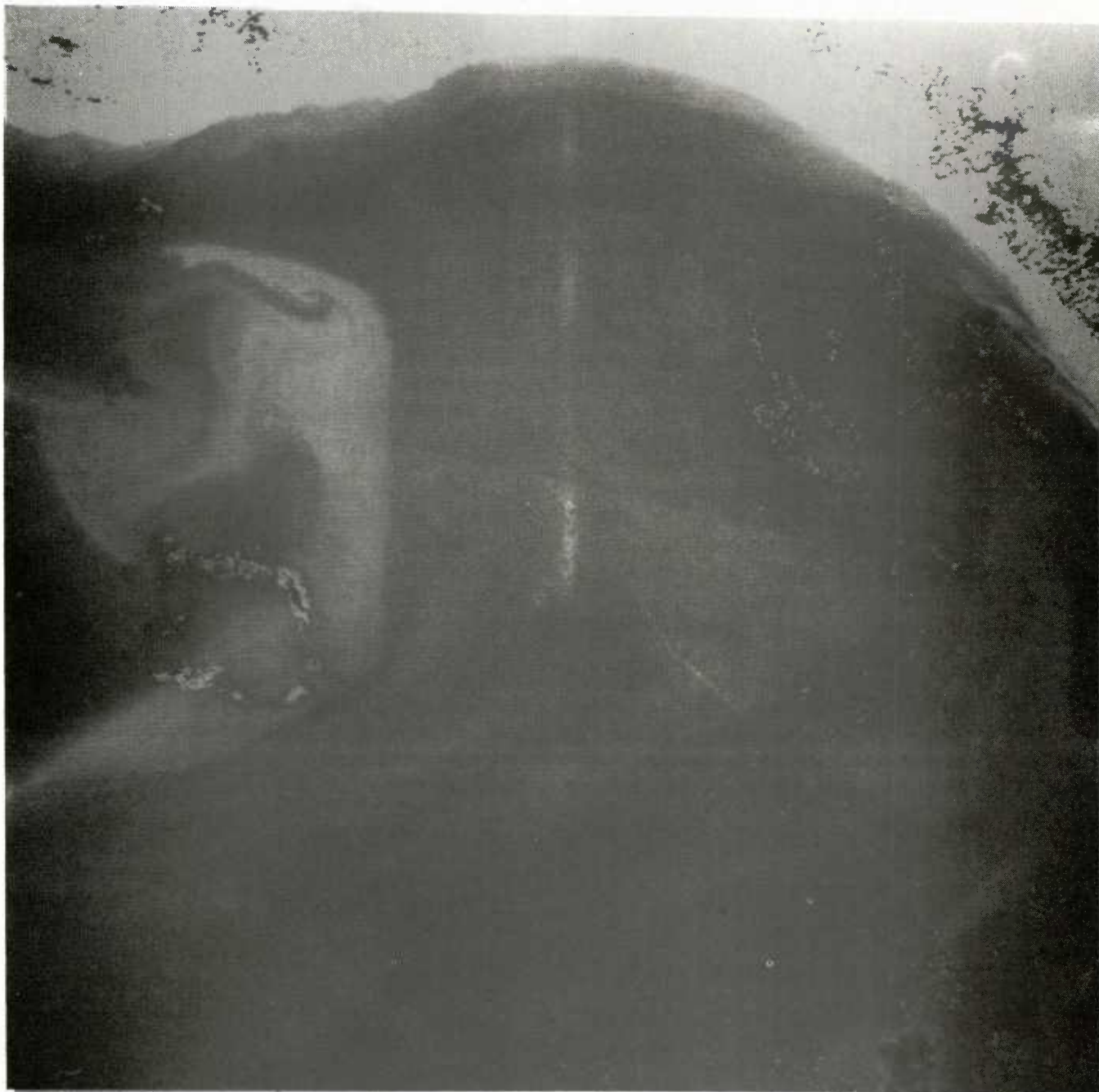


Figure 39. Image formed from application of the universal shelf-water algorithm (Eq. 8) to the image of Figure 37.

features through a warm, humid atmosphere that was opaque to IR sensors. The ability of the Nimbus-7 CZCS to see through these atmospheres where IR remote sensing of the ocean is ineffective is potentially important to the Navy.

Some consistency between the case studies indicates that universal algorithms for atmospheric correction based on a simple weighted sum of channels may be possible without going through the PCA procedure for every case. While not optimal, universal weighting coefficients for atmospheric correction by summing CZCS channels may be adequate for quick-look for Navy operational purposes. Coefficients for universal algorithms based on these four case studies have been proposed.

Other useful techniques have resulted from the study. For example, the aerosol path radiance has been associated with the first principal component of CZCS images when the PCA is performed. The first principal component that results is discarded to achieve an atmospheric correction. However, there are other Navy applications that might find the integrated aerosol scattering over the ocean as a desired parameter. In these cases, the first principal component of the PCA method may be useful in that, rather than being discarded as an unwanted contribution to the image, it would actually be the final product of the process indicating atmospheric aerosol concentrations.

7. References

- Angstrom, A. (1961). *Tellus*. 13, 214.
- Anderson, T. W. (1958). *An Introduction to Multivariate Statistical Analysis*. John Wiley & Sons.
- Austin, R. W. (1981). Solar Spectral Irradiances for CZCS channels 1-4. Technical Memorandum, Minutes of the Fifteenth CZCS NIMBUS Experiment Team Meeting, Monterey, California, January.
- Cooley, W. W. and P. R. Lohnes (1971). *Multivariate Data Analysis*. John Wiley & Sons.
- Duntley, S. Q., W. H. Wilson, and C. F. Edgerton (1974). Detection of Ocean Chlorophyll from Earth Orbit. *Ocean Color Analysis*, S. Q. Duntley, R. W. Austin, W. W. Wilson, C. F. Edgerton, and S. E. Moran, Eds. (Scripps Institution of Oceanography, U. California at San Diego), SIO Ref. 74-10.
- Frohlich, C. and G. E. Shaw (1980). New Determination of Rayleigh Scattering in the Terrestrial Atmosphere. *Appl. Opt.*, 19:11, pp. 1773-1775.
- Gordon, H. R. (1978). Removal of Atmospheric Effects from Satellite Imagery of the Oceans. *Appl. Opt.*, 17:10, pp. 1631-1636.
- Gordon, H. R. and D. K. Clark (1981). Clear Water Radiances for Atmospheric Correction of Coastal Zone Color Scanner Imagery. *Appl. Opt.*, 20:24, pp. 4175-4180.
- Hawkins, J. D. (1983). Satellite IR Data Utilization for Qualitative and Quantitative Observations of the Loop Current System. *EOS*, v. 64, n. 52, December.
- Hovis, W. A., D. K. Clark, F. Anderson, R. W. Austin, W. H. Wilson, E. T. Baker, D. Ball, H. R. Gordon, J. L. Mueller, S. Z. El-Sayed, B. Stum, R. C. Wrigley, and C. S. Yentsch (1980). Nimbus-7 Coastal Zone Color Scanner: System Description and Initial Imagery. *Science*, 210, pp. 60-63.
- Hurlburt, H. E. and J. Dana Thompson (1980). A Numerical Study of Loop Current Intrusion and Eddy Shedding. *J. Phys. Oceanogr.*, 10, pp. 1611-1651.
- Kinder, T. H. (1983). ¿Donde Va? An Oceanographic Experiment Near the Straits of Gibraltar. *Proceedings of IAPSO/ONR/NFKO Workshop on Straits Inst. Phy. Ocean.*, Copenhagen, Denmark.

Kneizys, F. X., E. P. Shettle, W. O. Gallery, J. H. Chetwynd, Jr., L. W. Abren, J. E. A. Selby, R. W. Fern, R. A. McClatchey (1980). Atmospheric Transmittance/Radiance: Computer Code LOWTRAN-5. AFGRL-TR-80-0067, Air Force Geophysical Laboratory.

La Violette, P. E. (1981). Variations in the Frontal Structure of the Southern Grand Banks. *NORDA TN #87*, April.

La Violette, P. E. (1983). Short-term Measurements of Surface Currents Associated with the Alboran Sea Gyre during ¿Donde Va?. *EOS*, v. 64, n. 18, p. 248.

La Violette, P. E. (1984). The Advection of Submesoscale Thermal Features in the Alboran Sea Gyre. Accepted for publication in *Journ. Phy. Ocean.*

La Violette, P., T. H. Kinder, R. Preller, and H. E. Hurlburt. ¿Donde Va?: A Mesoscale Flow Dynamics Experiment in the Straits of Gibraltar and Alboran Sea. XXVIIIth Congress and Plenary Assembly of ICSEM, Cannes, France, December 2-11 (in Proceedings).

Leipper, D. R. (1970). A Sequence of Current Patterns in the Gulf of Mexico. *JGR*, 75:3, pp. 637-657.

Mueller, J. L. and P. E. La Violette (1980). Color and Temperature Signatures of Ocean Fronts Observed with the NIMBUS-7 CZCS. Proceedings of COSPAR/SCOR/IUCRM Symposium, Oceanography from Space, Venice, Italy, May.

Neville, R. A., H. H. Zwick, J. R. Miller, and S. C. Jain (1980). Comparison of Suspended Solids and Chlorophyll Concentration Estimates from Aircraft and CZCS with In-Situ Measurements. IAMAP meeting, Radiation Transfer in the Oceans and Remote Sensing of Optical Properties, Hamburg, Germany, August.

Robinson, N., ed (1966). *Solar Radiation*. Elsev. Publ. Co., New York.

Smith, R. C. and W. H. Wilson (1981). Ship and Satellite Bio-Optical Research in the California Bight. *Oceanography from Space*, J. F. R. Gowen, Ed., Plenum Publishing Corp.

Tomasi, C. and F. Prodi (1982). Measurements of Atmospheric Turbidity and Vertical Mass Loading of Particulate Matter in Marine Environments (Red Sea, Indian Ocean, and Somalian Coast). *JGR*, 87:C2, pp. 1279-1286.

Distribution List

Commanding Officer
Naval Ocean R & D Activity
ATTN: Codes 100/111
NSTL MS 39529

Commanding Officer
Naval Ocean R & D Activity
ATTN: Code 125L
NSTL MS 39529

Commanding Officer
Naval Ocean R & D Activity
ATTN: Code 300
NSTL MS 39529

Commanding Officer
Naval Ocean R & D Activity
ATTN: Code 115
NSTL MS 39529

Commanding Officer
Naval Ocean R & D Activity
ATTN: Code 200
NSTL MS 39529

Commander
Naval Ocean Systems Center
San Diego CA 92152

Superintendent
Naval Postgraduate School
Monterey CA 93940

Commanding Officer
Naval Research Laboratory
Washington DC 20375

Commanding Officer
Naval Underwater Systems Center
ATTN: New London Lab
Newport RI 02840

Department of the Navy
Office of Naval Research
ATTN: Code 102
800 N. Quincy St.
Arlington VA 22217

Officer in Charge
Office of Naval Research
Detachment, Boston
Barnes Building
495 Summer St.
Boston MA 02210

Commanding Officer
ONR Branch Office LONDON
Box 39
FPO New York 09510

Commanding Officer
ONR Western Regional Ofcs
1030 E. Green Street
Pasadena CA 91106

Director
Scripps Inst of Oceanography
Univ of Southern California
La Jolla CA 92093

Working Collection
Texas A & M University
Department of Oceanography
College Station TX 77843

President
Woods Hole Oceanographic Inst
Woods Hole MA 02543

Department of the Navy
Asst Secretary of the Navy
(Research Engineering & System)
Washington DC 20350

Project Manager
ASW Systems Project (PM-4)
Department of the Navy
Washington DC 20360

Department of the Navy
Chief of Naval Material
Washington DC 20360

Department of the Navy
Chief of Naval Operations
ATTN: OP 951
Washington DC 20350

Department of the Navy
Chief of Naval Operations
ATTN: OP 987
Washington DC 20350

Director
Defense Technology Info Cen
Cameron Station
Alexandria VA 22314

Department of the Navy
Director of Navy Laboratories
Rm 1062 Crystal Plaza Bldg 5
Washington DC 20360

Commanding Officer
Fleet Numerical Ocean Cen
Monterey CA 93940

Commander
Naval Air Development Center
Warminster PA 18974

Commander
Naval Air Systems Command
Headquarters
ATTN: CAPT J. Ford
Washington DC 20361

Commanding Officer
Naval Coastal Systems Center
Panama City FL 32407

Commanding Officer
Naval Environmental Prediction
Research Facility
Monterey CA 93940

Commanding Officer
Naval Oceanographic Office
NSTL
Bay St. Louis MS 39522

Commander
Naval Oceanography Command
NSTL
Bay St. Louis MS 39522

Director, Liaison Office
Naval Ocean R&D Activity
800 N. Quincy Street
502 Ballston Tower #1
Arlington VA 22217

Mr. James Gallagher
Code 311
U.S. Navy Underwater Systems Center
New London CT 06333

Dr. James F. R. Gowen
Institute of Sciences
Patricia Bay
4860 West Saanich Road
P.O. Box 5000
Sidney, B.C. V8L 4B2 Canada

Mr. Charles McClain
Code 913
Goddard Space Flight Center
Greenbelt MD 20771

Mr. J. H. Richter
Naval Ocean Systems Center
Code 532
San Diego CA 92152

Mr. Tom Leming
National Marine Fisheries Service
NSTL MS 39529

Dr. Dennis Clark
NOAA/NESDIS S32
Washington DC 20233

Dr. John Walsh
Director, Oceanographic Sciences Division
Brookhaven National Laboratory
Upton NY 11973

Dr. Howard Gordon
Department of Physics
University of Miami
Coral Gables FL 33124

Dr. James Mueller
Department of Oceanography
Naval Post Graduate School
Monterey CA 93940

Dr. Otis Brown
MPO Division
University of Miami
4600 Rickenbacker Causeway
Miami FL 33149

Dr. Warren Hovis
NOAA/NESDIS S32
Washington DC 20233

Dr. Reuben Lasker
NOAA/NMFS
Southwest Fisheries Center
P.O. Box 271
La Jolla CA 92037

Mr. Marvin Blizard
Ocean Science & Technology Division
Office of Naval Research
800 N. Quincy St.
Arlington VA 22217

Robert Kirk
NASA Goddard Space Flight Center
Code 912
Greenbelt MD 20771

Dr. Roswell Austin
Visibility Laboratory
Scripps Institution of Oceanography
La Jolla CA 92093

Dr. Rudolph Hollman
Naval Ocean R&D Activity
Code 331
NSTL MS 39529

Dr. T. D. Allan
Institute of Oceanographic Sciences
Wormley, Godalming
Surrey, GU8 5UB
United Kingdom

Dr. M. Liepon
Lab d'Océanographie Physique du Muséum
43 rue Cuvier
75231 Paris CEDEX5
France

Madame Michele Champagne
ORSTOM
BPA5
Numia Cedse
New Caledonia

Dr. Heinz van der Peau
DFVLR
Oborpfaffenhofeu
8031 Wessling
Fed. Rep. of Germany

Department of the Navy
Chief of Naval Operations
ATTN: CAPT D. Honhart, OP-952D
Washington DC 20350

Commander
Naval Electronic Sys. Com. Hdqtrs.
ATTN: CDR D. McConathy
PME 106-48
Washington DC 20360

Dr. H. Dolezalek
Ocean Science & Technology Division
Office of Naval Research
800 N. Quincy st.
Arlington VA 22217

Director
National Ocean & Atmospheric Admin.
AOML
ATTN: Dr. George Maul
4301 Rickenbacker Causeway
Miami FL 33149

Director
NOAA (NESDIS)
5001 Silverhill Rd., Rm 318
Washington DC 20031

Commander
Naval Air Systems Command
Headquarters
ATTN: Dr. P. Twitchell, AIR-370
Washington DC 20361

Dr. R. L. Bernstein
CAL Space, A-021
University of California
Scripps Institution of Oceanography
La Jolla CA 92093

Dr. J. O'Brien
FSU Department of Meteorology
Meteorology Annex
Tallahassee FL 32306

U215431